Change of motion of a swimming droplet

Saori Suda

Abstract

Swimming microdroplets driven by the Marangoni effect attract attention because they are simple self-propelled models with fluidic features resembling living organisms, such as swimming cells. Several experiments of swimming droplets have reported that they not only move straightly but also exhibit more complex behavior. Although the theoretical understanding of these changes in motion has progressed, the effect of the mechanisms inside the droplet and the external perturbations has not been clarified. Therefore, we studied how the swimming droplet's internal mechanisms and external perturbations affect the droplet's motion. First, we experimentally studied the motion of the swimming water droplet when the droplet size is changed. As a result, the droplets tend to take more curved trajectories as their radii increase. Secondly, to clarify the relationship between curvilinear motion and higher hydrodynamic modes, we developed and analyzed a three-dimensional axis-asymmetric model consisting of the Stokes equation and an advection-diffusion equation with surfactant influx and outflux terms. We estimated the surfactant concentration on the surface by fitting the PIV results of the internal flow with the solution of the Stokes equation and quantitatively verified the consistency between the model and the experimental results. The analysis of the model suggested that the angular response to external perturbations changes depending on the droplet size. This is mainly caused by the change in the droplet size switching the swimming mode of the stable equilibrium solution with the straight motion from puller to pusher. We verified that the angular response to perturbations also affects the global behavior of the droplet by performing numerical simulations using the established model with the addition of perturbations. We introduced the thermal noise modeled by the white noise and a kind of sporadic noise to mimic the perturbation that is caused by the chemical trails. The numerical simulations with different types of noise showed that the detailed characteristics of the trajectories were different, although they are overall similar. Larger droplet size is expected to increase the frequency of the encounter with noise sources or events because it also increases the droplet's speed and surface area, so we conducted numerical simulations with varying the frequency of sporadic noise events. The results are consistent with the experimental results of larger-sized droplets as they show more curly trajectories and more oscillatory angular autocorrelation as the frequency increases. The obtained results suggested that the types and properties of external perturbation have a considerable effect on droplet motion.

Publication List

Published paper

Saori Suda, Tomoharu Suda, Takuya Ohmura, and Masatoshi Ichikawa, Straight-to-curvilinear motion transition of a swimming droplet caused by the susceptibility to fluctuations, *Physical Review Letters* 127, 088005 (2021).

Saori Suda, Tomoharu Suda, Takuya Ohmura, and Masatoshi Ichikawa, Motion of a swimming droplet under the external perturbations: a model-based approach, *Physical Review E* 106, 034610 (2022).

Related papers

Mariko Suga, Saori Suda, Masatoshi Ichikawa, and Yasuyuki Kimura, Self-propelled motion switching in nematic liquid crystal droplets in aqueous surfactant solutions, *Physical Review E* 97, 062703 (2018).

Charlotte de Blois, Vincent Bertin, Saori Suda, Masatoshi Ichikawa, Mathilde Reyssat and Olivier Dauchot, Swimming droplets in 1D geometries: an active Bretherton problem, *Soft Matter*, 17, 6646-6660 (2021).

Contents

Chapter 1

General introduction

1.1 Overview

Research on microswimmers, which are swimming bodies of micrometer scale such as microorganisms, has gained momentum in recent years [1, 2, 3, 4, 5]. Their motion is governed by physics in the low Reynolds number regime, where the viscous effect is stronger than the inertial effect, which leads to physics different from the macro world. The understanding of the physics of microswimmers is expected to lead to applications in bioengineering and environmental studies [6, 7]. Microswimmers include not only living organisms such as *Escherichia coli* and *Paramecium* but also nonliving ones including nanorods and Janus particles [8, 3, 4]. Among nonliving microswimmers, swimming isotropic microdroplets have attracted attention as a simple self-propelled model with fluidic features similar to living organisms such as cells [9, 10]. Further research will not only contribute to a better understanding of microswimmers, but also to technologies that can be utilized to transport micrometer-scale materials and to chemical engineering applications [11, 12, 13, 14, 15, 16, 17]

The swimming droplet is driven by the Marangoni effect. When the surfactant concentration at the interface is inhomogeneous, convection flow occurs due to tangential stress caused by the interfacial tension gradient (Fig. 1.1). This effect is called the Marangoni effect. Depending on how the Marangoni effect is generated, swimming droplets are generally classified into two types: reacting droplets, which swim by chemical reaction, and solubilizing droplets, which swim by dissolution. The latter, solubilizing droplet, is driven by the Marangoni effect caused by the slow dissolution of the inner liquid into the outer field consisting of a surfactant solution above the critical micelle concentration. Solubilizing droplets attract interest because of their simple composition and their ability to swim for a few hours [11, 9, 18, 19]. Several experiments have reported that these swimming droplets not only move straight ahead but also exhibit more complex behavior. For example, in an experimental system of a liquid crystal droplet, it has been shown that linear, random, and helical motions can be observed as the droplet size and velocity change [20]. It has also been shown that an increase in viscosity results in a straight to curvilinear transition [21]. Theoretical studies on such motion transitions have
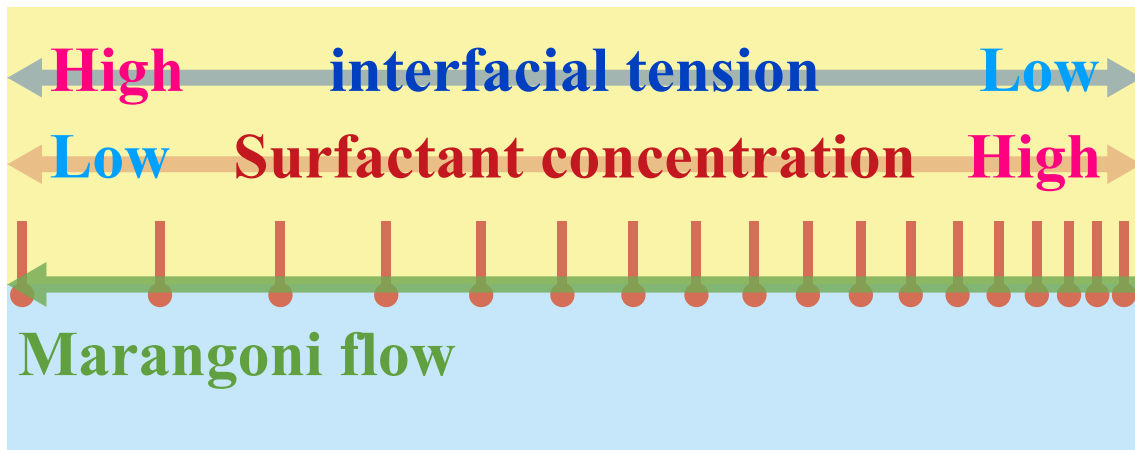
Figure 1.1: Schematic illustration of the Marangoni effect. When the surfactant concentration at the interface is inhomogeneous, convection flow occurs due to tangential stress caused by the interfacial tension gradient.

been progressing. For example, in a two-dimensional axisymmetric model, the dependence on the Péclet number, which represents the ratio between advection and diffusion effects, and the Damköhler number, which characterizes the strength of a chemical reaction, has been studied [22]. It has also been suggested that droplet motion is influenced not only by mechanisms inside the droplet but also by fluctuations in the external field and the randomness of interfacial reactions [23, 22]. Furthermore, it has been shown that droplets leave chemical traces while moving, which affect droplet motion [21, 24].

In this thesis, we report on research aimed to elucidate the mechanism of motion transition of a swimming droplet. In particular, we focused on the relationship between higher hydrodynamic modes or external perturbations and droplet motion, which had not been clarified in detail, and attempted both experimental and theoretical approaches. Specifically, we experimentally observed the motion of a droplet when the droplet size is changed, which had not been confirmed in the water-in-oil system. Additionally, we developed and analyzed a three-dimensional axis-asymmetric model consisting of the Stokes equation and an advection-diffusion equation with surfactant influx and outflux terms to clarify the relationship between curvilinear motion and higher hydrodynamic modes. Numerical simulations of the model with a noise term were also performed to clarify how external perturbations affect the complex motion of the droplet.

1.2 Swimming solubilizing droplet

1.2.1 Introduction of swimming solubilizing droplet

Swimming droplets driven by the Marangoni effect are generally classified into two types, reacting droplets and solubilizing droplets, depending on how the Marangoni

effect is induced [9, 10]. The former, reacting droplets, are driven by the Marangoni effect, which is caused by a chemical reaction that changes the structure of the surfactant molecule at the interface, thereby changing the active properties of its interfacial tension. The latter, solubilizing droplets, are driven by the Marangoni effect, which is caused by the slow dissolution of the internal liquid into the external field. In a surfactant solution above the critical micelle concentration, the droplet slowly dissolves and swollen micelles are formed. As a result, the local interfacial tension changes, and the Marangoni effect occurs. For the formation process of swollen micelles, two mechanisms have been proposed: first, direct interaction between the micelles and the interface leads to the formation of swollen micelles (micellar pathway); second, some of the droplet's constituent fluid molecules dissolve into the external field near the droplet interface, thereby forming swollen micelles (molecular pathway) [25]. The simplicity of this solubilizing droplet makes it useful for fundamental studies of droplet motion and interactions. Typical experimental systems are pure water droplets in a saturated squalane solution of monoolein and 4-pentyl-4'-cyanobiphenyl (5CB) oil droplets in a saturated aqueous solution of tetradecyltrimethylammonium bromide (TTAB) [11, 26, 27].

1.2.2 Governing equation of a swimming solubilizing droplet

The Stokes equation

Since the typical radius of swimming solubilizing droplets is tens to hundreds of μm and the typical velocity is a few to tens of μm/s, the effect of inertia can be neglected and their motion is described by the Stokes equation [9]. In the following, we derive the Stokes equation.

The Navier-Stokes equation for incompressible fluids without the body-forces is given by

$$\rho[\partial_t \mathbf{v} + (\mathbf{v} \cdot \nabla)\mathbf{v}] = -\nabla p + \eta \Delta \mathbf{v}, \tag{1.1}$$

where ρ is the mass density, $\mathbf{v}$ is the advection velocity, p is the pressure, and η is the dynamic viscosity. Let us consider its non-dimensionalization. Coordinates $\mathbf{r}$ and velocity $\mathbf{v}$ are expressed in terms of dimensionless coordinates $\bar{\mathbf{r}}$ and velocity $\bar{\mathbf{v}}$ as follows:

$$\mathbf{r} = L_0 \bar{\mathbf{r}}, \tag{1.2a}$$

$$\mathbf{v} = V_0 \bar{\mathbf{v}}, \tag{1.2b}$$

where L_0 is the characteristic length and V_0 is the characteristic velocity. Similarly, time t and pressure p are expressed in terms of dimensionless time $\bar{t}$ and pressure $\bar{p}$:

$$t = \frac{L_0}{V_0}\bar{t}, \tag{1.3a}$$

$$p = \frac{\eta V_0}{L_0}\bar{p}. \tag{1.3b}$$

Moreover, the derivatives are expressed in terms of dimensionless derivatives:

$$\partial_t = \frac{V_0}{L_0}\bar{\partial}_t, \tag{1.4a}$$

$$\nabla = \frac{1}{L_0}\bar{\nabla} \tag{1.4b}$$

By substituting Eqs. (1.2), (1.3), and (1.4) into Eq. (1.1), we obtain

$$Re[\bar{\partial}_t\bar{\mathbf{v}} + (\bar{\mathbf{v}} \cdot \bar{\nabla})\bar{\mathbf{v}}] = -\bar{\nabla}\bar{p} + \bar{\Delta}\bar{\mathbf{v}}, \tag{1.5}$$

where the dimensionless number Re (called the Reynolds number) is defined by

$$Re \equiv \frac{\rho V_0 L_0}{\eta}. \tag{1.6}$$

The Stokes equation is obtained as an the approximation when the Reynolds number is low:

$$0 = -\bar{\nabla}\bar{p} + \bar{\Delta}\bar{\mathbf{v}}, \tag{1.7}$$

where $\partial_t\mathbf{v}$ was assumed to be controlled by the intrinsic time scale L_0/V_0.

The Marangoni flow generated by a non-uniform surface tension profile at the droplet interface

Given a non-uniform interfacial tension distribution of the droplet, the flow field caused by the Marangoni effect can be calculated [28]. First, the Stokes equation is solved for a droplet fixed in space and a given non-uniform interfacial tension distribution (the resulting flow field is denoted $\mathbf{w}$). Next, the flow field $\mathbf{v}$ of a passive droplet swimming at a given velocity $\mathbf{v_D}$ is calculated. Then the complete flow field $\mathbf{u}$ of a swimming droplet is given by the superposition $\mathbf{u} = \mathbf{v} + \mathbf{w}$. Among the results of this calculation, we utilize Eqs. (2.4) and Eqs. (3.3) in this thesis.

The advection-diffusion equation and Péclet number

The transport of surfactant is described by the advection-diffusion equation

$$\partial_t c + \mathbf{v} \cdot \nabla c = D\Delta c, \tag{1.8}$$

where c is the concentration, $\mathbf{v}$ is the flow field, and D is the diffusion coefficient. The non-dimensionalization of this equation is similar to the case of the Navier–Stokes equation. By substituting Eqs. (1.2), (1.3), and (1.4) into Eq. (1.8), we obtain

$$\bar{\partial}_t c + \bar{\mathbf{v}} \cdot \bar{\nabla} c = \frac{1}{Pe}\bar{\Delta} c, \tag{1.9}$$

where the dimensionless number Pe (called the Péclet number) is introduced by

$$Pe = \frac{L_0 V_0}{D}. \tag{1.10}$$

1.2.3   Motion transition of swimming solubilizing droplet

In previous studies, it was experimentally indicated that the mode of motion of a swimming solubilizing droplet changes with swimming speed or with the viscosity of the solution around the droplets [20, 21]. In the system of 4-pentyl-4'-cyanobiphenyl (5CB) oil droplets in a saturated aqueous solution of tetradecyltrimethylammonium bromide (TTAB), a transition from random to helical and then to linear motion was observed as droplet size decreased at an approximately constant dissolution rate [20]. It has been shown that the transition from helical to linear motion is governed by the droplet speed, and that helical motion appears as the point defect of the droplet is displaced from the direction of motion of the droplet. In the system of a droplet of (S)-4-cyano-4'-(2-methylbutyl)biphenyl (CB15) in TTAB saturated water-glycerol mixtures in quasi-two-dimensional (Hele-Shaw cell) systems, the transition from quasiballistic to bimodal chaotic propulsion occurs by controlling the viscosity of the solution around the droplet [21]. The emergence of chaotic behavior is correlated with the emergence of higher hydrodynamic modes accompanying an increase in Péclet number due to increased viscosity. It has also been shown that when these higher hydrodynamic modes are dominant, the interaction with self-generating chemical gradients causes continual switching between the two modes of motion.

Theoretical investigations are also necessary to clarify the mechanism of motion transition of a swimming solubilizing droplet. Theoretical models of swimming droplets include those focusing on the phoretic forcing contribution and those focusing on droplet deformation [10, 29]. Moreover, there is a study in which numerical simulations have been conducted for a simple two-dimensional axisymmetric model that couples the Stokes equation with an advection-diffusion equation for the surfactant outside the droplet[1] [22]. There, it was shown that when the Péclet number is above a few tens, the coupling between the advection of the surfactant and the motion of the droplet strengthens with increasing Péclet number, and the motion transitions from steady translational motion to periodic and then to non-periodic motion. The droplet is also shown to oscillate between pusher and puller due to the interaction of secondary wake and primary wake and to move in zigzag trajectories formed by triangular, square, and mixed waves.

1.3   Outline of the thesis

This thesis reports on research aimed at elucidating the mechanism of motion transition of a swimming droplet. In particular, we focused on the relationship between higher hydrodynamic modes or external perturbations and droplet motion, the details of which have not been clarified. We elucidate them from both experimental and theoretical approaches.

In Chapter 2, we report on the results of experiments on pure water droplets in a saturated squalane solution of monoolein and the analysis of the model con-

---

[1]This study was published after the announcement of the main result of this thesis.

structed to clarify the mechanism of the phenomena observed in the experiments. The experimental results show that a straight to curvilinear transition occurs as the droplet size increases. To clarify the relationship between curvilinear motion and higher hydrodynamic modes, a three-dimensional axis-asymmetric model consisting of the Stokes equation and an advection-diffusion equation with surfactant influx and outflux terms was developed. A comparison of the model with experimental results indicated that the model is valid when the droplet radius is approximately less than 200 μm. Then, an analysis of the model by applying the parameters of the actual experimental system suggested that the angular response to the external perturbation changes with droplet size.

In Chapter 3, we explain the details of the derivation of the model developed in Chapter 2 and perform numerical simulations of the model with a noise term to discuss how external perturbations contribute to the complex motion of the droplet. First, we introduced a noise term to represent the characteristics of the noise in the concentration field or chemical trails. Second, we numerically calculated the sporadic noise with varying frequencies of noise events. The results suggested that the angular response to external perturbations affects the global behavior and that the type and characteristics of the noise affect the droplet motion.

In Chapter 4, we conclude the thesis and indicate some future works for research of swimming droplets.

Chapter 2

Straight-to-curvilinear motion transition of a swimming droplet

2.1 Introduction

At the end of the 19th century, G. Quinke presented self-propelled droplets as a model system for a migrating cell in an aqueous environment [30, 31]. It was stated that the fluid convection inside and outside of the swimming droplet is similar to that observed in the protoplasmic streaming of the amoeba cell [32]. Today, scientists understand that the droplet systems are not living cells themselves because their chemical systems are significantly different. However, physical and fluid-dynamical essentialities show common characteristics with both systems, such as roll convection, and their behaviors should be elucidated more with the fluid dynamics of a self-propelled object [33, 34, 28, 35, 36], physics of collective motions [2, 9], and force balance of adhesion and surface tension under non-equilibrium conditions [37].

In recent decades, there has been an increased interest in the spatio-temporal organization of self-propelled elements called active matters, such as swarms of fishes, birds, animals, and microorganisms. It is expected that the recognition of the physical phenomena that are unique to spontaneous and collective motions can be applied to various fields involving statistical physics, chemical technology, and life sciences [2, 3, 38]. Swimming droplets have been reexamined as an artificial active matter system with the special property that its motility is controllable using chemical means [9]. The motion of droplets induced by the Marangoni effect and wetting phenomena have been studied from the viewpoint of fundamental sciences [39, 40] and reaction control engineering [41, 42, 43]. While the driving forces in these systems have been actively studied, the understanding of motion controls, such as chemotactic motion [44] and spontaneous changes in motility, remains a challenging task. Additionally, swimming droplets are still significant as models of single and collective motion of living organisms. For example, various "living" motions are observed even in individual droplets [45, 11, 9, 46, 21, 18]. However, the emergence of motion diversity is not clearly understood.

Several examples of the motilities of swimming droplets have been reported.

Liquid crystals enable us to extract a specific mode of motion by controlling the symmetry inside the droplets [47, 48, 20, 49], where straight, curvilinear, and spiral motions, and their transitions, were demonstrated. As a simpler case, spontaneous symmetry-breaking of the motion of a swimming droplet in a two-dimensional system was investigated both experimentally [50, 51] and theoretically [52], which identified the straight-to-curvilinear motion transition. Recent experimental studies reported that an increase of the external surfactant concentration or the viscosity of the swimming medium causes the curvilinear motion of a swimming spherical droplet [46, 21]. In addition, the previous studies showed the existence of a relation between the emergence of the complex motion and the onset of higher hydrodynamic modes [21, 53]. However, the exact connection is not yet explicitly confirmed.

In this study, we measured the motion and internal flow of a spherical swimming water micro-droplet, and quantitatively identified a straight-to-curvilinear motion transition. To reveal the relationship between the curvilinear motion and the higher hydrodynamic modes, we developed a three-dimensional axis-asymmetric (torque-free) model consisting of an advection-diffusion equation, with influx and outflux of surfactants, coupled with the Stokes equation and investigated it analytically.

Experiments were conducted with following the previous study, where the individual droplets continued active swimming motion for more than 30 minutes [11]. Water is solubilized by reverse micelles in the oil phase (Fig. 2.1(a)). The droplets are driven by the Marangoni effect, induced by the inhomogeneity of the surface tension or surface coverage of the surfactants, which correlate to the solubilization rate and concentration of swollen reverse micelles nearby [54, 11]. A schematic illustration of the swimming mechanism is shown in Fig. 2.1(b).

2.2 Methods

Experiments were conducted with water droplets dispersed in oil that included a dissolved surfactant. Squalane oil (99%, Aldrich) with 25 mM 1-oleoyl-rac-glycerol (99%, Sigma) solution was filled in a sample chamber (with a 10 mm inner diameter and 2 mm height, made of a glass sheet floor and silicon sheet wall). The critical micellar concentration (CMC) for MO in Sq is 1.5 mM [45]. We used an electro-microinjector (FemtoJet 4i, Eppendorf) to generate spherical pure water droplets to control the volume and number of droplets (Fig. 2.2). The procedure is the same as in a previous study [20]. Water droplets larger than the mechanical limit of the injector (radius $R \gtrsim 200~\mu$m) were formed by manual pipetting. To eliminate interactions between the water droplets, the number of droplets placed in the chamber was restricted to no more than five. The motion of the water droplets was observed using an inverted bright-field microscope (Ti-E, Nikon) with x1, x4, and x20 magnification objective lenses, and was captured at 10 frames/s using a complementary metal-oxide-semiconductor camera (ORCA-Flash 4.0, Hamamatsu). Fig. 2.3 shows a schematic illustration of the experimental method. For visualization of the flow inside the droplets, 1-μm-diameter polystyrene beads (Fluoresbrite PolyFluor 497 Microspheres, Polysciences, Inc.) were used as probes for the flow, and the vector
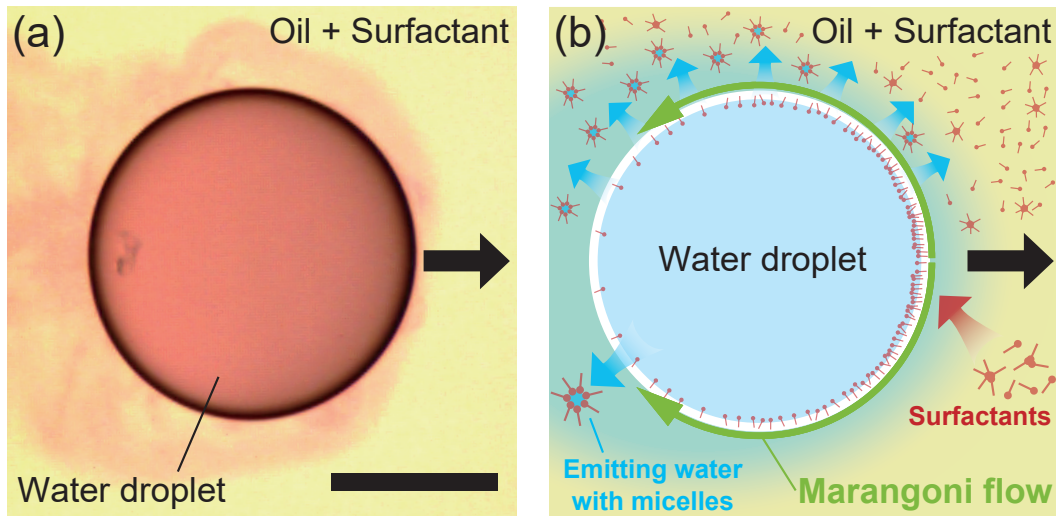
Figure 2.1: (a) Solubilization of water around a swimming droplet. The water is dyed using Acid Red 52 (Tokyo Chemical Industry Co., Ltd.). The red color gradient around the droplet shows that the stained water inside the droplet was being emitted. The black arrow represents the direction of the droplet's movement. The scale bar represents 200 μm. (b) Schematic illustration of the swimming mechanism of a droplet. The droplet is driven by the Marangoni flow (green arrows) generated by the solubilization of water (blue arrows).

fields were measured via particle imaging velocimetry with PIVlab in MATLAB (Mathworks) [55]. All experiments were conducted at ambient temperature (25°C).

2.3 Experimental Results

In Fig. 2.4(a), typical trajectories of the centroids of the droplets are represented for three different radii scales. Fig. 2.4(b) displays the trajectories of the centroids of the droplets for $30 \lesssim R \lesssim 400$ μm.

The droplets tend to take more curved trajectories as their radii increase. To confirm this observation quantitatively, we calculated the angular autocorrelation function $\langle C(t,\tau) \rangle_t$ of the direction of movement of the droplets with velocity $\mathbf{v}(t)$, which is given as a function of lag time τ: $\langle C(t,\tau) \rangle_t = \left\langle \frac{\mathbf{v}(t+\tau) \cdot \mathbf{v}(t)}{|\mathbf{v}(t+\tau)||\mathbf{v}(t)|} \right\rangle_t$, where $\langle \rangle_t$ represents the time average, and a three-point moving average was applied to the velocity (Fig. 2.3(a)). The group of fastest relaxations (red lines) attained minimum at $\tau \sim 2.8$ s, and its half $\tau_{\min} = 1.4$ s was a suitable lag time to identify degree of curved motion as $\arccos C(t, \tau_{\min})$. Qualitatively similar behavior has been observed in other experimental systems [46, 21]. The oscillatory motion of the large droplets is possibly related to the chaotic motion shown in a previous study [53]. To quantify the persistence of the straight motion, we introduced the decay time of $\langle C(t,\tau) \rangle_t$ by fitting with that of the Brownian harmonic oscillator $\langle C(t,\tau) \rangle_t = e^{-a_1\tau+a_2} \cos a_3\tau$ [56]. The decay time $1/a_1$ was plotted as a function of the droplet radius, which
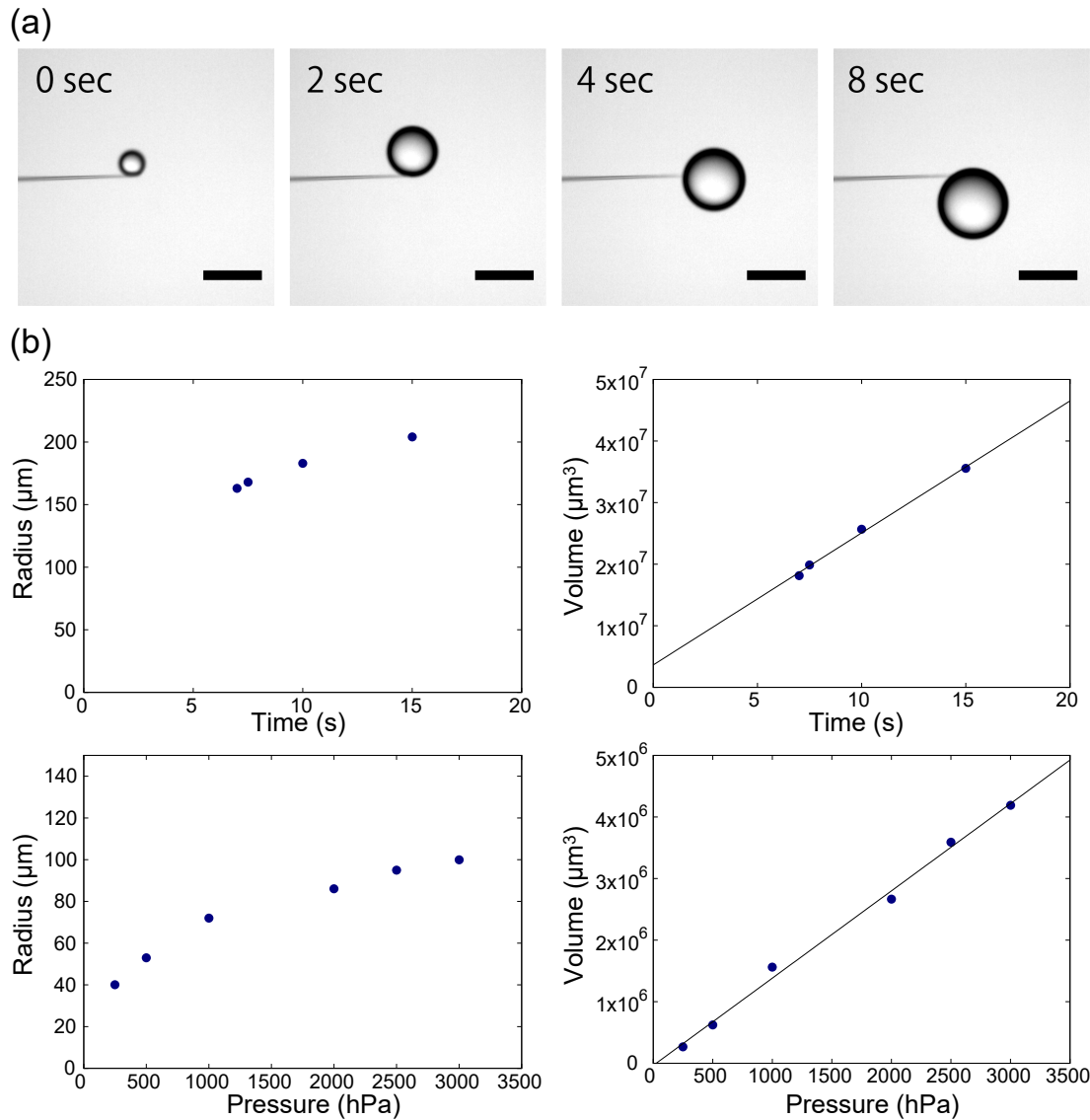
Figure 2.2: (a) Photograph of the electro-microinjector producing a water droplet. The scale bar represents 200 μm. (b) The size of water droplets produced by varying the application pressure and time of an electro-microinjector. The graph showing the radius of the produced droplets (left). The graph showing the volume of the produced droplets (right). The application pressure is fixed at 5000 hPa (top). The application time is fixed at 5 s (bottom).
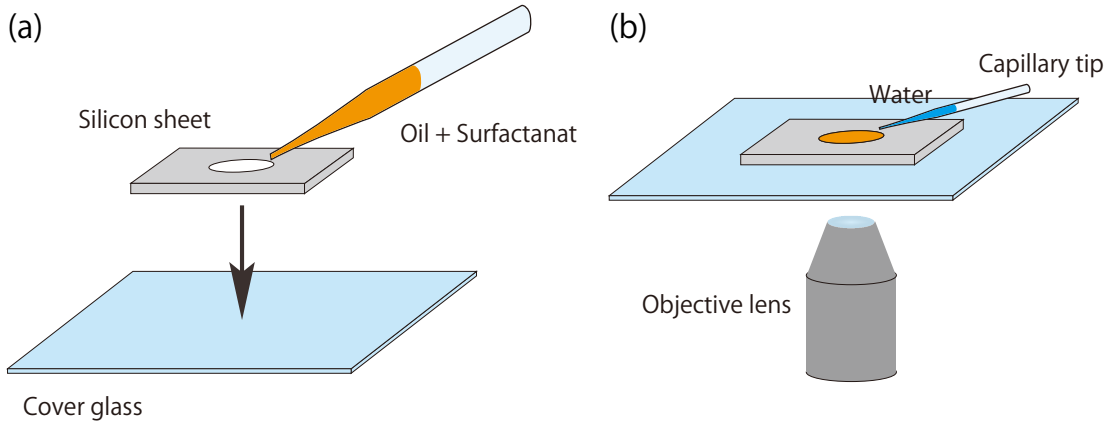
Figure 2.3: Schematic illustration of the experimental method. (a) A silicon sheet with a hole is pressed onto a cover glass, and oil with surfactant solution is poured into the created chamber. (b) Water droplets were produced in oil with surfactant solution using an electro-microinjector and observed from below using an inverted bright-field microscope.

indicated that the decay times tend to change at approximately $R \approx 100$ μm (Fig. 2.3(b)). The average speed increased with the radius and saturated at $R \approx 100$ μm (Fig. 2.3(c)).

Fig. 2.6 shows typical results of the flow inside the droplets in the equatorial plane measured through particle imaging velocimetry (PIV) experiment. Besides dipolar flow, quadrupolar flow was observed for some droplets with $R \gtrsim 200$ μm when they turned. Furthermore, the PIV experiment evaluated contributions of the flow modes (Fig. 2.8(b)) and especially the difference angle between the axes of dipolar and quadrupolar flow fields, which corresponds $\Psi/2$ as we see later analysis. The systematic correlation between the difference angle Ψ and the turning angle of movement of the droplet (Fig. 2.8(a)) suggests that the angle plays an essential role in the transition of the motion.

2.4 Theoretical Model

To validate this hypothesis and explain the mechanism of the transition, we developed a three-dimensional axis-asymmetric theoretical model, based on a theoretical study of a swimming droplet driven by the Marangoni flow in a two-dimensional system [52]. The velocity of the droplets was assumed to lie in the horizontal plane in agreement with the experimental observations. In constructing the model, we considered the flow on the surface of the droplets instead of the internal flow, which is determined by the surfactant concentration on the droplet surface [28].

The surfactant concentration $c(\theta, \phi)$ on the droplet surface, parametrized by the polar angle θ and azimuthal angle ϕ, is assumed to obey,
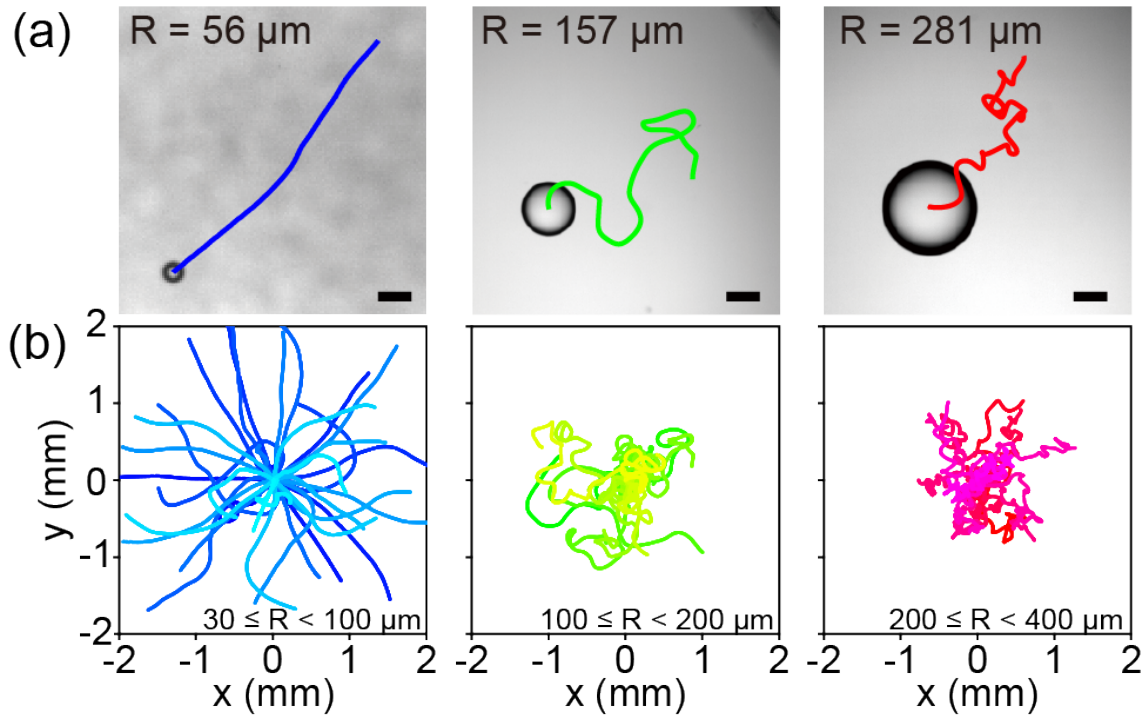
Figure 2.4: Trajectories of the centroids of the swimming droplets over 60 seconds. (a) The typical trajectories of the droplet centroids. The radii of the water droplets are 56 μm (left), 157 μm (middle), and 281 μm (right). The scale bars represent 200 μm. (b) Trajectories of the centroids of the droplets for three categories of droplet radii. The starting points are set to the origin. The radii categories are $30 \leq R < 100$ μm (left), $100 \leq R < 200$ μm (middle), and $200 \leq R < 400$ μm (right). Color variation depicts different droplets.

$$\frac{\partial c}{\partial t} + \mathbf{u} \cdot \nabla c = \frac{D}{R^2}\Delta_{\text{sphere}}c - \alpha c + \alpha\beta\delta\left(\theta - \frac{\pi}{2}, \phi - \arg\frac{\mathbf{v}}{|\mathbf{v}|}\right), \qquad (2.1)$$

where α and β are the characteristic duration of stay on the surface and the relative rate of the supply of the surfactant, $\mathbf{u}$ is the flow field on the droplet surface, D is the diffusion coefficient of the surfactant on the surface, and $\Delta_{\text{sphere}} = \frac{1}{\sin\theta}\frac{\partial}{\partial\theta}\left(\sin\theta\frac{\partial}{\partial\theta}\right) + \frac{1}{\sin^2\theta}\frac{\partial^2}{\partial\phi^2}$ is the Laplacian operator on the unit sphere.

We expand the surfactant concentration c and the flow field $\mathbf{u}$ in terms of spherical harmonics Y_l^m using the solution of the Stokes equation in terms of the surface tension distribution (given in Section 3.5) [28]. The terms with lower-degree spherical harmonics are retained so that the flow field inside the droplet is symmetrical in the horizontal plane, as the droplet was not moving significantly in the vertical direction and our focus here is the angle between the axes of dipolar and quadrupolar flows. Thus we expand c as $c(\theta, \phi) = c_1^{-1}Y_1^{-1} + c_1^1Y_1^1 + c_2^0Y_2^0 + c_2^{-2}Y_2^{-2} + c_2^2Y_2^2$, where $c_1^{-1} = -(c_1^1)^*$ and $c_2^{-2} = -(c_2^2)^*$ are complex numbers, and c_2^0 is a real number. On the equatorial plane, the term with $(l, m) = (1, \pm1)$ yields a dipolar flow, $(2, 0)$ a
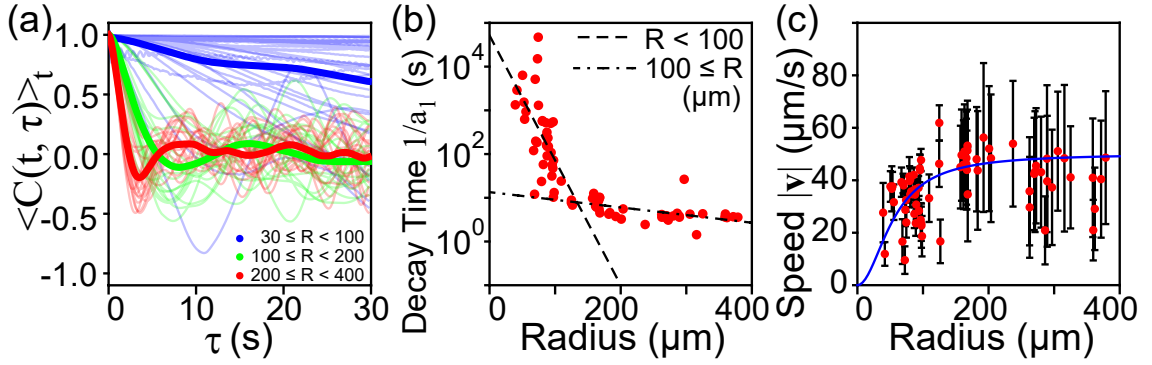
Figure 2.5: Analysis of the experimental results. (a) Angular autocorrelation function $\langle C(t,\tau)\rangle_t$ of the direction of movement of the droplets. The thin lines correspond to the individual droplets, and the thick lines show the ensemble averages of the droplets in the respective size categories. (b) Droplet radius dependence of the decay time $\langle C(t,\tau)\rangle_t$. Each black dashed line represents an exponential fitting line for the data points with $R < 100~\mu$m and $\geq 100~\mu$m. (c) Droplet radius dependence of the time-averaged speed of the droplets (red dots). Error bars represent the standard deviations of the speed. The blue line is a fitting curve using Eq. (3.24) with $R < 250~\mu$m.

radial flow, and $(2,\pm2)$ a quadrupolar flow. Fig. 8 shows the streamlines of the flow fields in the equatorial plane of the spherical droplets when the surfactant concentration c is respectively represented only by the components $(l, m) = (1, \pm1)$, $(2, 0)$ or $(2, \pm2)$. We set the retained terms as $c_1^1 = \rho e^{i\nu}$, $c_2^0 = Z$, and $c_2^2 = \mu e^{i\lambda}$, where $\rho > 0$ and $\mu > 0$. The variables ρ and $\pi - \nu$ correspond to the strength and the direction of the "dipolar flow", respectively. Further, ρ and ν determine the velocity of the droplet [28]:

$$\mathbf{v} = \frac{1}{3}\sqrt{\frac{6}{\pi}}\frac{\gamma\rho}{2\eta + 3\hat{\eta}}\begin{pmatrix} -\cos\nu \\ \sin\nu \\ 0 \end{pmatrix}, \tag{2.2}$$

where η is the oil viscosity, $\hat{\eta}$ is the water viscosity, and γ is a factor of proportionality between surface tension and concentration. Similarly, μ and $\pi - \lambda/2$ correspond to the strength and the direction of the "quadrupolar flow".

From Eq. (2.1) and the solution of the Stokes equations, we obtain a system of ordinary differential equations governing the motion of the droplet (the derivation is described in Section 3.2). Nondimensionalization yields a system of equations:
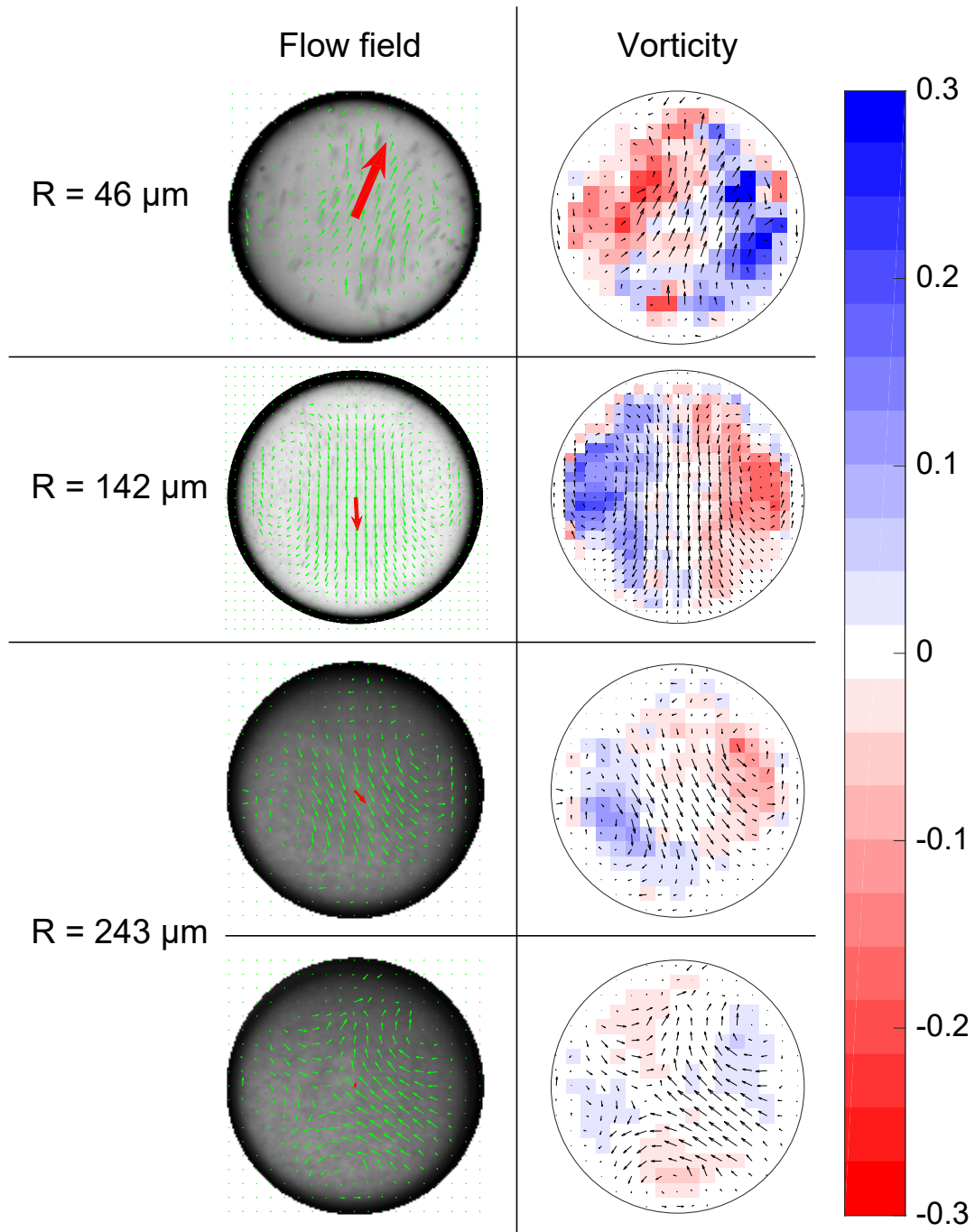
Figure 2.6: Typical results of the internal flow in each size of the droplet measured through PIV. In the left column, the flow fields are shown. The small green arrows represent the flow fields. The thick red arrows represent the velocity of the droplets, and the lengths of them were normalized by the droplets radii. In the right column, the vorticities of the flow fields are shown. The two figures at $R = 243\ \mu$m represent the flow field at different times of the same droplet.

Figure 2.7: The streamlines of the flow fields in the equatorial plane of the spherical droplets when the surfactant concentration c is respectively represented only by the components $(l, m) = (1, \pm1), (2, 0)$ or $(2, \pm2)$. We calculated them with the solution of the Stokes equation in terms of the surface tension [28].
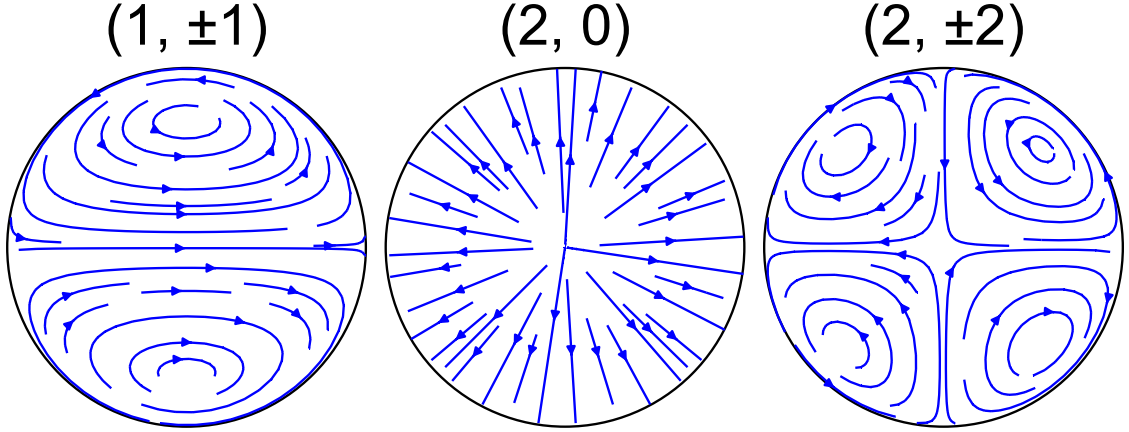
$$\frac{d\bar{\rho}}{d\bar{t}} = -\frac{3}{10\bar{R}}\sqrt{\frac{5}{\pi}}(1 + \chi)\left(-\sqrt{6}\bar{\rho}\bar{\mu}\cos(\lambda - 2\nu) + \bar{\rho}\bar{Z}\right)$$
$$- \left(1 + \frac{2L^2}{\bar{R}^2}\right)\bar{\rho} + \frac{1}{4}\sqrt{\frac{6}{\pi}}, \tag{2.3a}$$

$$\frac{d\nu}{d\bar{t}} = \frac{3}{10\bar{R}}\sqrt{\frac{30}{\pi}}(1 + \chi)\bar{\mu}\sin(\lambda - 2\nu), \tag{2.3b}$$

$$\frac{d\bar{Z}}{d\bar{t}} = \frac{1}{35\bar{R}}\sqrt{\frac{5}{\pi}}(7\bar{\rho}^2 + 15\chi\bar{Z}^2 - 30\chi\bar{\mu}^2) - \left(1 + \frac{6L^2}{\bar{R}^2}\right)\bar{Z} - \frac{1}{4}\sqrt{\frac{5}{\pi}}, \tag{2.3c}$$

$$\frac{d\bar{\mu}}{d\bar{t}} = \frac{1}{40}\sqrt{\frac{30}{\pi}}\left(-\frac{4\bar{\rho}^2}{\bar{R}} + 5\right)\cos(\lambda - 2\nu) - \frac{6}{7\bar{R}}\sqrt{\frac{5}{\pi}}\chi\bar{Z}\bar{\mu}$$
$$- \left(1 + \frac{6L^2}{\bar{R}^2}\right)\bar{\mu}, \tag{2.3d}$$

$$\frac{d\lambda}{d\bar{t}} = -\frac{1}{40}\sqrt{\frac{30}{\pi}}\left(-\frac{4\bar{\rho}^2}{\bar{R}} + 5\right)\frac{\sin(\lambda - 2\nu)}{\bar{\mu}}, \tag{2.3e}$$

where the overlined symbols denote nondimensionalized quantities. The parameter $L = l_d/l_a$ is determined by constants $l_d = \sqrt{D/\alpha}$ and $l_a = \gamma\beta/\alpha(2\eta + 3\hat{\eta})$, corresponding to the characteristic lengths of diffusion and advection, respectively. The parameter $\chi = (2\eta + 3\hat{\eta})/(5\eta + 5\hat{\eta})$ is calculated as 0.41 using the values of the viscosity of squalane 28.33×10^{-3} kg/(m · s) [57] and water 0.89×10^{-3} kg/(m · s) (0.1 MPa, 25 °C). The parameter $L = D/2\pi L v_\infty l_d$ is calculated as 0.0082 by fitting the speed of droplets with Eq. (3.24) using experimental results.

2. Straight-to-curvilinear motion transition of a swimming droplet

To quantitatively verify the consistency between the model and the experimental results, we estimated the surfactant concentration in the surface c_l^m from the observed flow field by fitting the PIV results of the internal flow with the solution of the Stokes equation in terms of $\rho, \nu, Z, \mu,$ and λ. The measured flow inside the droplet was fitted using the least-squares method with the solution of the Stokes equation around the spherical droplet in terms of the surface tension $\sigma = \Sigma_{(l,m)}^\infty s_l^m Y_l^m$ [28]:

$$\hat{u}_r = \frac{-\eta}{2(\eta+\hat{\eta})}\left[\frac{r^2}{R^2}-1\right]\mathbf{e}_r\cdot\mathbf{v}^D + \frac{1}{\eta+\hat{\eta}}\sum_{l=1}^\infty\sum_{m=-l}^l\left[\frac{r^{l+1}}{R^{l+1}}-\frac{r^{l-1}}{R^{l-1}}\right]\frac{l(l+1)s_l^m}{4l+2}Y_l^m, \quad (2.4a)$$

$$\hat{u}_\theta = \frac{-\eta}{2(\eta+\hat{\eta})}\left[\frac{2r^2}{R^2}-1\right]\mathbf{e}_\theta\cdot\mathbf{v}^D + \frac{1}{\eta+\hat{\eta}}\sum_{l=1}^\infty\sum_{m=-l}^l\left[(l+3)\frac{r^{l+1}}{R^{l+1}}-(l+1)\frac{r^{l-1}}{R^{l-1}}\right]\frac{s_l^m}{4l+2}\partial_\theta Y_l^m, \quad (2.4b)$$

$$\hat{u}_\varphi = \frac{-\eta}{2(\eta+\hat{\eta})}\left[\frac{2r^2}{R^2}-1\right]\mathbf{e}_\varphi\cdot\mathbf{v}^D + \frac{1}{\eta+\hat{\eta}}\sum_{l=1}^\infty\sum_{m=-l}^l\left[(l+3)\frac{r^{l+1}}{R^{l+1}}-(l+1)\frac{r^{l-1}}{R^{l-1}}\right]\frac{ims_l^m}{4l+2}\frac{Y_l^m}{\sin\theta}, \quad (2.4c)$$

where $x = r\sin\theta\cos\phi$, $y = r\sin\theta\sin\phi$, and $z = r\cos\theta$. We reconstructed the vector fields using the variables $c_1^1 = \rho e^{i\nu}$, $c_2^0 = Z$, and $c_2^2 = \mu e^{i\lambda}$, and the residual flow field was defined by the difference between the reconstruction and the observation. The relative strength of each term was estimated from the norm of each vector field (Fig. 2.8(b)). The residual was large when $R \lesssim 50$ μm, possibly caused by the insufficient resolution of the image. When $R \gtrsim 50$ μm, as the droplet radius increased, the quadrupolar terms $(2,0)$ and $(2,\pm2)$ became dominant, while the dipolar term $(1,\pm1)$ diminished. The residual also increased due to higher-degree terms.

Speeds of the droplets in the experiments are compared with ones predicted by Eq. (2.2) using values of $\gamma\rho$ estimated from the PIV results (Fig. 2.8(c)). The speed was observed to be proportional to $\gamma\rho$ for $R < 200$ μm (green dots), distributed along the blue line representing the model with the same viscosity values as above.

Angular velocities are also estimated from the dimensional version of Eq. (2.3b). We obtain a relation $\frac{d\nu}{dt} = \frac{3}{50}\sqrt{\frac{30}{\pi}}\frac{7\eta+8\hat{\eta}}{(\eta+\hat{\eta})(2\eta+3\hat{\eta})}\frac{\gamma\mu\sin\Psi}{R}$, where $\Psi = \lambda - 2\nu$. Fig. 2.8(d) displays a scatter plot between the angular velocity of the motion vector of the droplet adopting $\arccos C(t,\tau_{\min})/\tau_{\min}$ and $\gamma\mu\sin\Psi/R$ evaluated from the PIV experiments. The distribution normalized by $\gamma\mu\sin\Psi/R$ for $R < 200$ μm (green dots) suggests a master curve, and that is represented by the above equation without free fitting parameters (blue line), i.e., the model is consistent with the PIV result.

To investigate the possible scenarios of the motion transition, we conducted a linear stability analysis for Eqs. (2.3). Solutions of stable straight motion should satisfy $d\nu/d\bar{t} = 0$, i.e., $\sin\Psi = 0$. This is further classified into two cases $\Psi = 0$ and $\Psi = \pi$. Using the effective squirmer parameter $\frac{3\sqrt{3}}{20\bar{\rho}}\left(\sqrt{6}\bar{\mu}\cos\Psi - \bar{Z}\right)$ [28], we see that $\Psi = 0$ and $\Psi = \pi$ corresponds to puller and pusher squirmer types, respectively, if $\bar{Z}$ is small. For $\Psi = 0$ and $\Psi = \pi$, we numerically calculated $\bar{\rho}, \bar{Z}, \bar{\mu}$ of Eqs. (2.3) and the eigenvalues of the coefficient matrices of the linearized systems. A result consistent with the experiment is obtained using the value $D = 10^{-10}$ m^2/s. There
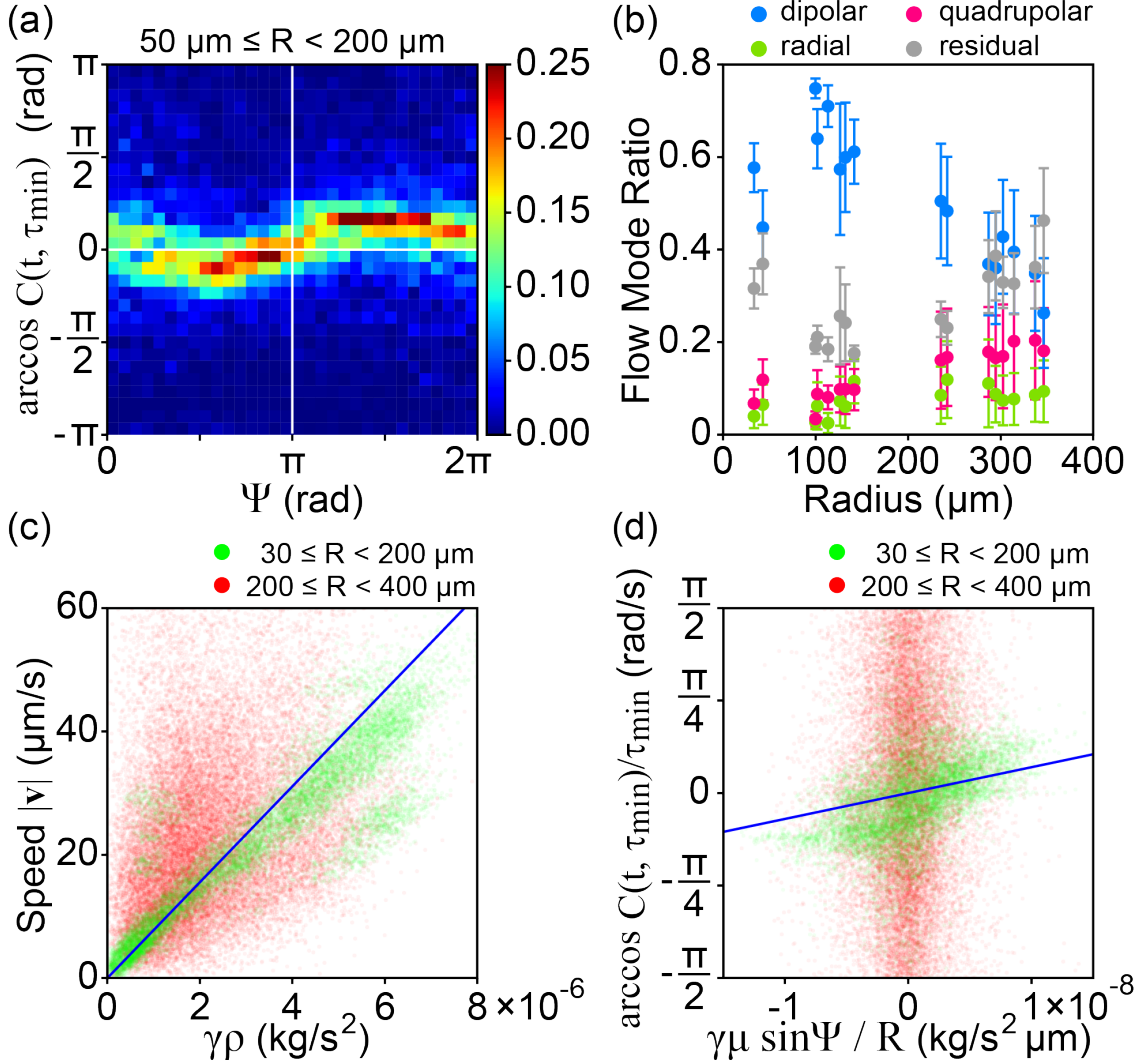
Figure 2.8: Results of PIV experiments. The flow modes were extracted from PIV data of the internal flow, and were calculated into the concentration mode of the chemical ρ, μ, λ, etc. (a) 2D density map between the difference angle $\Psi = \lambda - 2\nu$ and degree of curved motion as $\arccos C(t, \tau_{\min})$. The color indicates the density. (b) The average ratio of flow modes observed in the PIV experiments, i.e., $(l, m) = (1, \pm 1)$: dipolar, $(2, 0)$: radial, $(2, \pm 2)$: quadrupolar, and the residual flow fields, given by the norm of each vector field, on the droplet radius. Error bars represent the standard deviations of the ratios. (c) Scatter diagram between the speed of the droplet $|\mathbf{v}|$ and model suggested parameter $\gamma\rho$ estimated from the PIV results. The green dots represent $30 < R < 200$ μm and red dots represent $200 \leq R < 400$ μm. The model denotes the blue line as $v = 7.77 \times 10^6 \times \gamma\rho$ μm s^{-1}. (d) Scatter diagram between angular velocity $\arccos C(t, \tau_{\min})/\tau_{\min}$ and $\gamma\mu \sin\Psi/R$. The green and red dots represent the same range as those of (c). The blue line is predicted by the present model without free fitting parameters as $\frac{d\nu}{dt} = 2.20 \times 10^7 \times \frac{\gamma\mu\sin\Psi}{R}$ rad s^{-1} .

23

are stable solutions with $\Psi = 0$ for $R \lesssim 34\,\mu$m (Fig. 2.9(a-1)), and with $\Psi = \pi$ for $R \gtrsim 34\,\mu$m (Fig. 2.9(a-2)). Although both are stable, the growth of the perturbation is different.

The rate of increase of the deviation from the solution is defined by $\Delta\nu_\infty = M\Delta\nu_0$ with a stimulus $\Delta\nu_0$ and the following response $\Delta\nu_\infty$. In the $\nu - \lambda$ plane, the trajectory of the solution of the system of ordinary differential equations (2.3) is described by the following equation:

$$\frac{d\lambda}{d\nu} = \frac{A_2}{A_1},\qquad(2.5)$$

where

$$\frac{d\nu}{d\bar{t}} = A_1 \sin\Psi = \frac{3}{10\bar{R}}\sqrt{\frac{30}{\pi}}(1+\chi)\bar{\mu}\sin\Psi,\qquad(2.6\text{a})$$

$$\frac{d\lambda}{d\bar{t}} = A_2 \sin\Psi = -\frac{1}{40\bar{\mu}}\sqrt{\frac{30}{\pi}}\left(-\frac{4\bar{\rho}^2}{\bar{R}}+5\right)\sin\Psi.\qquad(2.6\text{b})$$

If A_1 and A_2 are assumed to be constant, we obtain

$$\lambda(\nu) = \frac{A_2}{A_1}(\nu - \nu_0) + \lambda_0,\qquad(2.7)$$

where (ν_0, λ_0) is the initial value for (ν, λ). By the stability of equilibrium solutions, the final state of the system $(\nu_\infty, \lambda_\infty)$ is an equilibrium solution if the perturbation is small enough. Let the initial value be $(\nu_0 + \Delta\nu_0, \lambda_0)$, where (ν_0, λ_0) is an equilibrium solution. Let us first consider the case of $\Psi = 0$. In this case, equilibrium solutions satisfy $\Psi = \lambda - 2\nu = 0$. Therefore, we have

$$\lambda_0 = 2\nu_0,\qquad(2.8\text{a})$$
$$\lambda_\infty = 2\nu_\infty.\qquad(2.8\text{b})$$

On the other hand, we have

$$\lambda_\infty = \lambda(\nu_\infty) = \frac{A_2}{A_1}(\nu_\infty - \nu_0 - \Delta\nu_0) + \lambda_0,\qquad(2.9)$$

from (2.7). Solving (2.8) - (2.9) for ν_∞, we obtain

$$\nu_\infty = \nu_0 + \frac{A_2}{A_2 - 2A_1}\Delta\nu_0.\qquad(2.10)$$

Because $\Delta\nu_\infty = \nu_\infty - \nu_0$, the coefficient M is $A_2/(A_2 - 2A_1)$. The calculation for the case $\Psi = \pi$ is similar. Fig. 2.9(b) shows the coefficient M at a stable solution of straight motion as a function of the droplet radius. If $M < 1$, a delayed effect accompanied by an external stimulus $\Delta\nu_0$ is rapidly damped and a straight motion restarts. If $M > 1$, the effect leaves an imprint on the direction of movement for a longer time, and it gradually turns toward $\sim M\Delta\nu_0$. Actually, numerical simulation
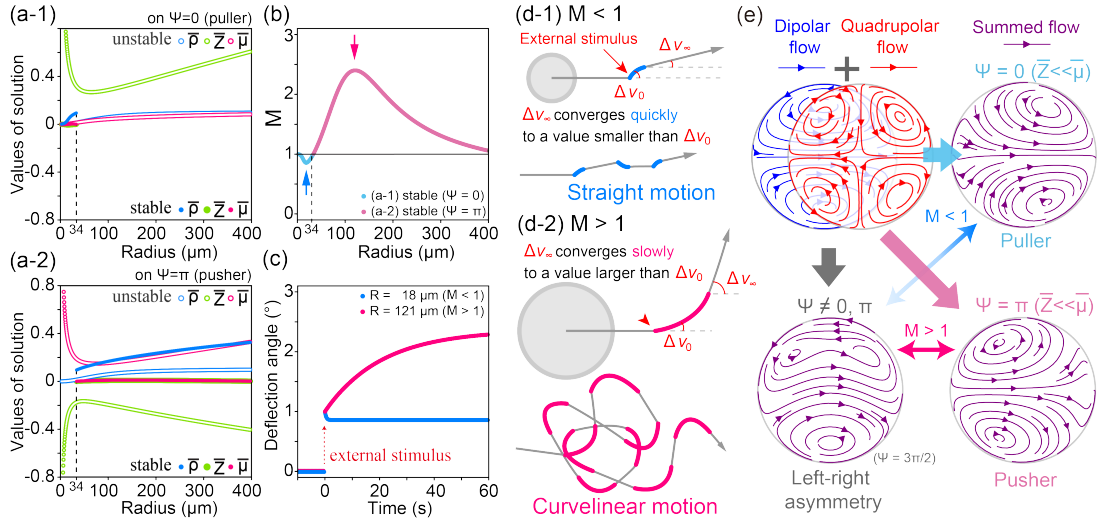
Figure 2.9: Analysis of solutions of straight motion for the diffusion coefficient $D = 10^{-10}$ m^2/s. (a) Values and stability of solutions of $\Psi = 0$: puller (a-1) and $\Psi = \pi$: pusher (a-2). (b) Multiplier coefficient M of motion direction against stimulus versus droplet radius R. (c) Time development of the direction of movement of the droplet from the initial direction when the external stimulus 1° is applied to the direction of movement. For the stable solution of straight motion at radius $R = 18$ μm (blue) and $R = 121$ μm (magenta). (d) Schematic illustrations of motions of droplets under stimuli in real space with $M < 1$ (d-1) and > 1 (d-2). (e) Schematic diagram of the internal flow modes of the droplet.

of Eqs.(2.3) confirms the significantly longer relaxation time in the case of $M > 1$ than $M < 1$, and total deflection angles in droplet movements are magnified by $\sim M$ (Fig. 2.9(c)). Time developments of the respective motions under stimuli will differ phenomenologically (Fig. 2.9(d)).

This responsiveness transition from $M < 1$ to $M > 1$ occurs around the radius $R \approx 34$ μm as a result of the change of swimming mode between puller and pusher for the stable straight solution (Fig. 2.9(a)). Size of the droplet is one of essential parameters to elevate the strengths of quadrupolar-flow and -concentration, therefore changes of stability and responsiveness of the direction of the quadrupolar flow occur due to the droplet size variance. Since deviation of Ψ from the solutions 0 and π corresponds left-right asymmetrical flow (Fig. 2.9(e)), effective periods exhibiting the asymmetrical flow accompanied by turning motion is enlarged by the property $M > 1$ (Fig. 2.9(d)). Apart from external stimuli such as thermal fluctuation, an internal perturbation is possibly induced by the self-generated chemical ununiformity [21]. From the above discussion, we conclude that the observed motion transition is precisely the transition of the angular response to perturbations.

2.5 Conclusion

There are two fundamental transitions observed in self-propelled objects: stationary-moving and straight-curvilinear [54, 46, 21, 50, 51, 52]. In particular, the latter transition is essential to the motion diversity. We experimentally and theoretically revealed that even an isotropic swimming droplet, which has spherical symmetry, exhibits a straight-to-curvilinear motion transition. Considering the simplicity of the experimental system and the present model, it is probable that similar orbital instability in straight swimming movement exists in a phase separation [40] and in a living cell such as an amoeboid swimmer [30, 31, 58, 59, 60]. Further study in this line would be of interest, as it may reveal a mechanism behind the rich variety of living and active motions in nature.

2.6 Appendix

Equilibrium solutions and their stability

We numerically calculated for each equilibrium solution $\bar{\rho}$, $\bar{Z}$, and $\bar{\mu}$ of Eqs. (2.3) and $\max(Re(k_i))$, where k_i are the eigenvalues of the coefficient matrices of the linearized system for equilibrium solutions. If $\max(Re(k_i)) < 0$, then all the eigenvalues have negative real parts and therefore the corresponding equilibrium solution is stable. At $D = 10^{-9}$ m^2/s, a line of stable equilibrium solutions is yielded for $\Psi = 0$ with $0 < R < 400$ μm. At $D = 10^{-10}$ m^2/s, lines of stable equilibrium solutions exist. In Fig. 2.10, we show the results when the diffusion coefficient D is from 10^{-9} m^2/s to 10^{-12} m^2/s.
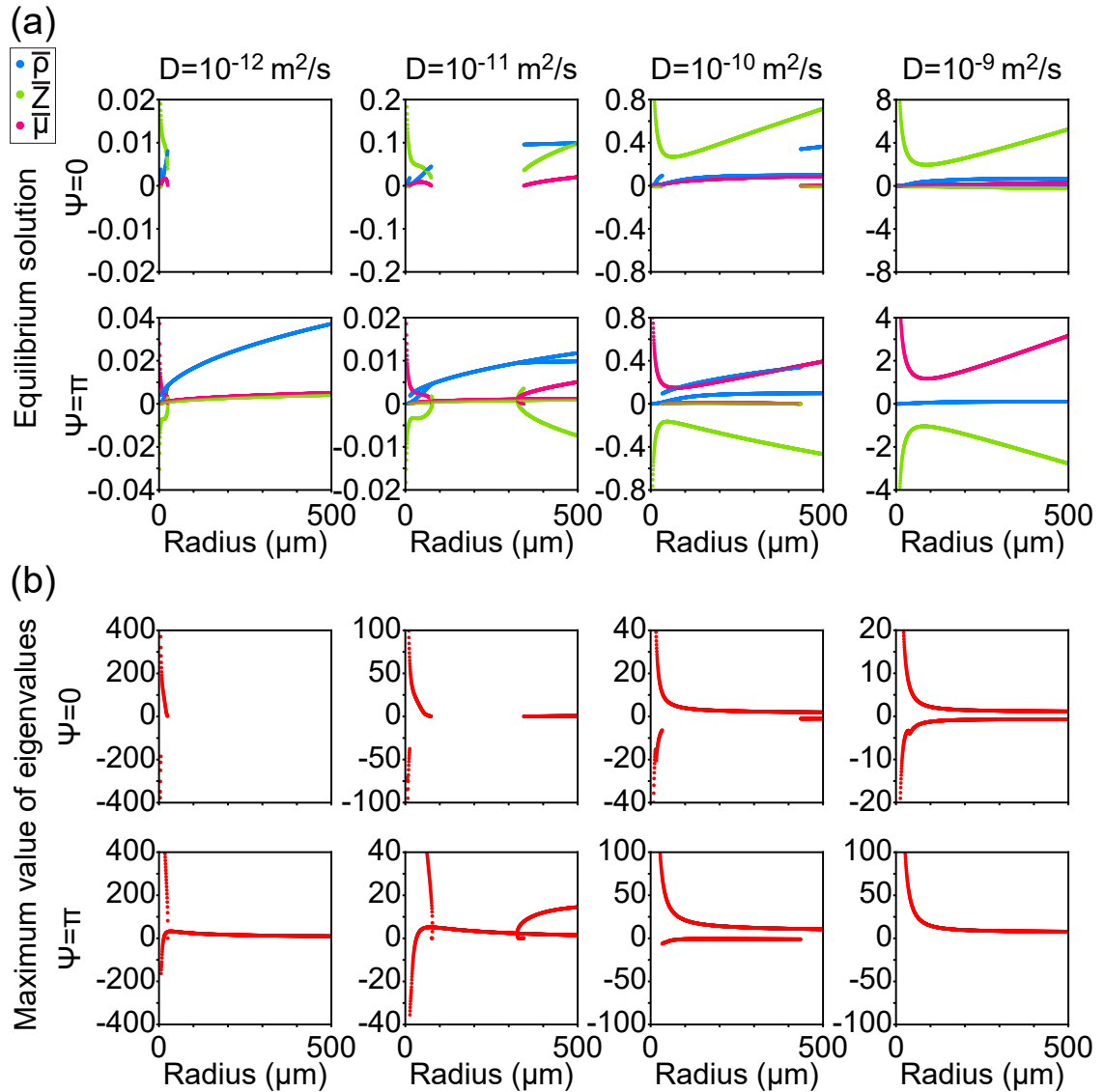
Figure 2.10: Analysis of equilibrium solutions when the diffusion coefficient D is from 10^{-9} m²/s to 10^{-12} m²/s. (a) Values of equilibrium solutions for $\Psi = 0$ and $\Psi = \pi$. (b) Graph of $\max(Re(k_i))$, where k_i are the eigenvalues of the coefficient matrices of the linearized system for equilibrium solutions for $\Psi = 0$ and $\Psi = \pi$. If $\max(Re(k_i)) < 0$, then all the eigenvalues have negative real parts; therefore, the corresponding equilibrium solution is stable.

Chapter 3

Motion of a swimming droplet under external perturbations

3.1 Introduction

Microswimmers such as swimming microorganisms are strongly affected by viscosity, which has various implications in the physical characteristics of their motion [8, 61]. In recent years, there has been an increase in the research activities on microswimmers [1, 2, 3, 4, 5]. The fluid dynamics based on the behavioral patterns of microswimmers will open up the potential for widespread applications in bioengineering and environmental studies [6, 7]. There are many non-living microswimmers such as Janus particles [4, 62]. In particular, swimming microdroplets have recently gained significant attention because they are self-propelled simple models with fluidic features that resemble living organisms such as swimming cells [32]. Further research will not only deepen our understanding of microswimmers, but also lead to the development of applications in chemical engineering [13, 14, 15, 16, 17]. Swimming microdroplets driven by the Marangoni effect are suitable for practical applications because they tend to swim for hours despite their simple composition [11, 9, 18, 19, 10]. The Marangoni effect here is caused by the slow dissolution of the internal liquid into an external surfactant solution that is more concentrated than the critical micelle concentration. It has been experimentally demonstrated that the motion of the swimming microdroplet changes from straight to curvilinear, and further to chaotic, with an increase in the Péclet number $Pe = UR/D_o$, where U is the characteristic speed, R is the droplet radius, and D_o is the diffusion coefficient of surfactants on the outside field [20, 46, 19, 21].

Theoretical elucidation of these changes in motion has been progressing. An axially symmetric model has been proposed that focuses on the adsorption of surfactants at the surface caused by dissolution, whereby it has been found that two types of qualitatively different droplet behaviors may be stabilized [53]. In a two-dimensional axis-asymmetric model, Li has studied the dependence of the motion of droplets on the Péclet number and the Damköhler number, which characterizes the strength of chemical reactions [22]. It has been suggested that the motion is affected

not only by the mechanism inside the droplet, but also by fluctuations in the external field and the randomness of the interfacial reaction [23, 22]. Since the droplet moves curvilinearly while leaving a chemical trail, the chemical trail affects the droplet motion as an external perturbation [21, 24]. The authors have constructed a three-dimensional axis-asymmetric model, by combining an advection-diffusion equation with the inflow and outflow of the surfactant and the Stokes equation, and its correspondence with the experiment was confirmed [19]. The analysis suggests that the angular response to perturbations changes depending on the droplet size.

The purpose of the current study is to investigate the effect of external perturbations on droplets driven by the Marangoni effect to consider the contribution of external perturbations to the complex motion of droplets and the influence of droplet size on this effect. We first give a detailed explanation of the derivation of the model that was introduced in a previous study [19], which is used to describe the motion of a droplet. This model is a system of ordinary differential equations, and it is relatively easy to analyze. We then study the angular response to random perturbations using numerical methods based on the model to consider how external noises affect the motion of droplets and how the motion mechanism of droplets contributes to it. Accordingly, we introduce random noises with different characteristics so that the stimuli present in experimental settings are mimicked.

3.2 Derivation of the model

In this section, we provide a detailed derivation of the three-dimensional axis-asymmetric model proposed and outlined in a previous study[19]. For mathematical notations used in the derivation, see Section 3.5. The model describes the droplet motion in terms of ordinary differential equations with five variables, which represent the mode of the surfactant distribution at the droplet surface. To describe the concentration of surfactant at the droplet surface, we consider an advection-diffusion equation with the terms representing the inflow and outflow of surfactant, and couple it with the Stokes equation. By expanding the concentration and the flow using the spherical harmonics Y_l^m and leaving only the terms with degree and order $(l, m) = (1, \pm 1), (2, 0)$, and $(2, \pm 2)$, five ordinary differential equations are obtained. On the equatorial plane, the term with $(l, m) = (1, \pm 1)$ yields a dipolar flow, $(2, 0)$ a radial flow, and $(2, \pm 2)$ a quadrupolar flow.

The model is given as follows:

$$\frac{d\bar{\rho}}{d\bar{t}} = -\frac{3}{10\bar{R}}\sqrt{\frac{5}{\pi}}(1+\chi)\left(-\sqrt{6}\bar{\rho}\bar{\mu}\cos(\lambda-2\nu)+\bar{\rho}\bar{Z}\right)-\left(1+\frac{2L^2}{\bar{R}^2}\right)\bar{\rho}+\frac{1}{4}\sqrt{\frac{6}{\pi}}$$

(3.1a)

$$\frac{d\nu}{d\bar{t}} = \frac{3}{10\bar{R}}\sqrt{\frac{30}{\pi}}(1+\chi)\bar{\mu}\sin(\lambda-2\nu)$$

(3.1b)

$$\frac{d\bar{Z}}{d\bar{t}} = \frac{1}{35\bar{R}}\sqrt{\frac{5}{\pi}}(7\bar{\rho}^2+15\chi\bar{Z}^2-30\chi\bar{\mu}^2)-\left(1+\frac{6L^2}{\bar{R}^2}\right)\bar{Z}-\frac{1}{4}\sqrt{\frac{5}{\pi}}$$

(3.1c)

$$\frac{d\bar{\mu}}{d\bar{t}} = \frac{1}{40}\sqrt{\frac{30}{\pi}}\left(-\frac{4\bar{\rho}^2}{\bar{R}}+5\right)\cos(\lambda-2\nu)-\frac{6}{7\bar{R}}\sqrt{\frac{5}{\pi}}\chi\bar{Z}\bar{\mu}-\left(1+\frac{6L^2}{\bar{R}^2}\right)\bar{\mu}$$

(3.1d)

$$\frac{d\lambda}{d\bar{t}} = -\frac{1}{40}\sqrt{\frac{30}{\pi}}\left(-\frac{4\bar{\rho}^2}{\bar{R}}+5\right)\frac{\sin(\lambda-2\nu)}{\bar{\mu}},$$

(3.1e)

where $\bar{R}$ is the normalized radius of the droplet, and L and χ are the parameters defined in Subsection 3.2.3 that describe the physical properties of the droplet system. The variables $\bar{\rho}, \nu, \bar{Z}, \bar{\mu}$ and λ describe the modes of distribution of surfactant on the surface of the droplet, which determines the convection inside and outside the droplet. In terms of the corresponding distribution, $\bar{\rho}$ and ν correspond to the first-degree spherical harmonics and $\bar{Z}, \bar{\mu}$ and λ the second degree (the definitions are given in Eqs. (3.18)). The motion of the droplet can be described in terms of these quantities. For instance, the velocity of the droplet can be reconstructed from $\bar{\rho}$ and ν using Eq. (3.23).

The authors have demonstrated that the predictions from the present model are consistent with the experimental results for radii less than 200 μm, under the choice of parameters estimated from experimental results [19].

Later in this study, we perform numerical simulations using the present model to analyze the effect of perturbations on droplet motion.

3.2.1 Basic assumptions

Droplets are driven by the Marangoni effect. Conversely, the motion of the droplets induces a gradient in the surfactant concentration because the droplet constantly moves toward a fresh solution, and leaves a trail of a waste product (swollen micelle)-rich solution [25, 9, 10]. We incorporate this effect by introducing a supply term limited to the pole at the direction of motion.

Because no significant vertical motion was observed in the experiments, we assume that the velocity of the droplets lies in the horizontal plane [19]. Under these considerations, the dynamics of the concentration c of the surfactant on the surface is modeled by an advection-diffusion equation of the form

$$\frac{\partial c}{\partial t} + \mathbf{u} \cdot \nabla c = \frac{D}{R^2}\Delta_{\text{sphere}}c - \alpha c + \alpha\beta\delta(\theta-\frac{\pi}{2},\phi-\arg\mathbf{v}^D),$$

(3.2)

where $\mathbf{u}$ is the flow field on the droplet surface, D is the diffusion coefficient of the surfactant on the surface, α is the inverse of the characteristic duration of stay on the surface, and β is the relative rate of supply of the surfactant, $\Delta_{\text{sphere}} = \frac{1}{\sin\theta}\frac{\partial}{\partial\theta}\left(\sin\theta\frac{\partial}{\partial\theta}\right) + \frac{1}{\sin^2\theta}\frac{\partial^2}{\partial\phi^2}$ is Laplacian operator on the unit sphere, $\mathbf{v}^D = (v_x, v_y, 0)^T$ is the velocity of the droplet, and δ is the delta function. The function $\arg\mathbf{v}^D$ is defined as the argument of the vector $\mathbf{v}^D = (v_x, v_y, 0)^T$ lying in the horizontal plane when interpreted as a complex number $v_x + iv_y$.

Internal flow field and external flow field are described by the addition of solutions for the Stokes equation corresponding to pumping active droplet and passive droplet, respectively [28]. The formula for these flow fields are given in terms of the surface tension σ, the viscosity outside the droplet η, viscosity inside the droplet $\hat{\eta}$, and radius of the droplet R as the parameters. According to the result, the flow field $\mathbf{u}$ on the droplet surface is described by

$$u_r = 0, \tag{3.3a}$$

$$u_\theta = \frac{-\eta}{2(\eta + \hat{\eta})}\mathbf{e}_\theta \cdot \mathbf{v}^D + \frac{1}{\eta + \hat{\eta}}\sum_{l=1}^{\infty}\sum_{m=-l}^{l}\frac{s_l^m}{2l+1}\partial_\theta Y_l^m, \tag{3.3b}$$

$$u_\varphi = \frac{-\eta}{2(\eta + \hat{\eta})}\mathbf{e}_\varphi \cdot \mathbf{v}^D + \frac{1}{\eta + \hat{\eta}}\sum_{l=1}^{\infty}\sum_{m=-l}^{l}\frac{ims_l^m}{2l+1}\frac{Y_l^m}{\sin\theta}, \tag{3.3c}$$

where $\sigma = \Sigma_{l,m}^{\infty}s_l^m Y_l^m$ is the spherical harmonics expansion of the surface tension distribution, and the velocity of the droplet $\mathbf{v}^D$ is defined as

$$\mathbf{v}^D = \sqrt{\frac{1}{6\pi}}\frac{1}{2\eta + 3\hat{\eta}}\begin{pmatrix} s_1^1 - s_1^{-1} \\ i(s_1^1 + s_1^{-1}) \\ -\sqrt{2}s_1^0 \end{pmatrix}. \tag{3.4}$$

The Stokes equation and advection-diffusion equation (3.2) are coupled by a proportional relation between the concentration and the surface tension described by

$$\sigma = \sigma_0 - \gamma c, \tag{3.5}$$

where $\gamma > 0$ is the constant of proportionality. A similar treatment of the coupling was studied for a two-dimensional droplet [52, 22].

3.2.2   Expansion of flow field and concentration of surfactant

First, we expand the concentration c and the flow field $\mathbf{u}$ using spherical harmonic functions, in order to obtain reduced ordinary differential equations from Eq. (3.2).

The expansion of the concentration is straightforward, from which we obtain

$$c = \sum_{l=0}^{\infty}\sum_{m=-l}^{l}c_{lm}Y_l^m, \tag{3.6}$$

where

$$c_{lm} = \int_0^{2\pi} \int_0^\pi c(\phi, \theta)(Y_l^m)^* \sin\theta \, \mathrm{d}\theta \, \mathrm{d}\phi \,. \tag{3.7}$$

Using the expression for the gradient in polar coordinates, the Eqs. (3.3) can be rewritten into the following concise form:

$$\mathbf{u} = \sum_{l=0}^\infty \sum_{m=-l}^l U_{lm} R \nabla Y_l^m. \tag{3.8}$$

In this expression, the coefficients U_{lm} are given by

$$U_{11} = \frac{\eta}{(\eta + \hat\eta)} \sqrt{\frac{\pi}{6}} (v_x - iv_y) + \frac{1}{3(\eta + \hat\eta)} s_{11} = \frac{s_{11}}{2\eta + 3\hat\eta}, \tag{3.9a}$$

$$U_{1-1} = \frac{-\eta}{(\eta + \hat\eta)} \sqrt{\frac{\pi}{6}} (v_x + iv_y) + \frac{1}{3(\eta + \hat\eta)} s_{1-1} = \frac{s_{1-1}}{2\eta + 3\hat\eta}, \tag{3.9b}$$

and

$$U_{lm} = \frac{1}{\eta + \hat\eta} \frac{s_{lm}}{2l + 1} \tag{3.10}$$

if $l \geq 2$.

Because the coefficients U_{lm} are given in terms of s_{lm}, we may alternatively represent them in terms of c_{lm} using the proportionality relation (3.5).

3.2.3 Expansion of the advection-diffusion equation

Next, we use the results in Subsection 3.2.2 in Eq. (3.2) to obtain reduced ordinary differential equations.

The main problem is the advection term, which is nonlinear and therefore some consideration is required to deal with it. However, because $\mathbf{u} \cdot \nabla c$ is a scalar function on a sphere, we may expand it as follows.

$$\mathbf{u} \cdot \nabla c = \sum_{l=0}^\infty \sum_{m=-l}^l A_{lm} Y_m^l. \tag{3.11}$$

Consequently, we obtain a system of ordinary differential equations, which describes the dynamics of the droplet:

$$\frac{dc_{lm}}{dt} + A_{lm} = -\left(\alpha + l(l+1)\frac{D}{R^2}\right) c_{lm} + \alpha\beta \sqrt{\frac{2l+1}{4\pi} \frac{(l-m)!}{(l+m)!}} P_l^m(0) e^{-im \arg \mathbf{v}^D}. \tag{3.12}$$

Let us determine the unknown coefficients A_{lm}. Using the expressions obtained in Subsection 3.2.2, we calculate as follows.

$$\mathbf{u} \cdot \nabla c = \left(\sum_{r=0}^\infty \sum_{s=-r}^r U_{rs} R \nabla Y_r^s\right)\left(\sum_{p=0}^\infty \sum_{q=-p}^p c_{pq} \nabla Y_p^q\right)$$
$$= \frac{1}{R} \sum_{r=0}^\infty \sum_{s=-r}^r \sum_{p=0}^\infty \sum_{q=-p}^p U_{rs} c_{pq} R^2 \left(\nabla Y_r^s \cdot \nabla Y_p^q\right). \tag{3.13}$$

By multiplying both sides with $(Y_l^m)^*$ and integrating over the unit sphere, we obtain

$$A_{lm} = \frac{1}{R} \sum_{r=0}^{\infty} \sum_{s=-r}^{r} \sum_{p=0}^{\infty} \sum_{q=-p}^{p} G_{lm}^{pqrs} U_{rs} c_{pq}, \qquad (3.14)$$

where

$$G_{lm}^{pqrs} = \int_0^{\pi} \int_0^{2\pi} \sin\theta \left(R\nabla Y_r^s \cdot R\nabla Y_p^q \right) (Y_l^m)^* d\phi d\theta. \qquad (3.15)$$

The coefficients G_{lm}^{pqrs} can be regarded as describing the strength of coupling between different modes of the distribution of the surfactant, and it is easy to show the following properties:

$$G_{lm}^{pqrs} = 0 \quad \text{if} \quad q + s \neq m, \qquad (3.16a)$$
$$G_{lm}^{pqrs} = G_{lm}^{rspq} \quad \text{for all} \quad p, q, r, s, l, m. \qquad (3.16b)$$

The lowest degree and order independent terms of G_{lm}^{pqrs} are calculated as follows.

$$G_{11}^{221-1} = -\frac{3}{10}\sqrt{\frac{30}{\pi}}, \qquad (3.17a)$$

$$G_{11}^{1120} = -\frac{3}{10}\sqrt{\frac{5}{\pi}}, \qquad (3.17b)$$

$$G_{20}^{222-2} = -\frac{3}{7}\sqrt{\frac{5}{\pi}}, \qquad (3.17c)$$

$$G_{20}^{111-1} = -\frac{1}{10}\sqrt{\frac{5}{\pi}}, \qquad (3.17d)$$

$$G_{20}^{2020} = \frac{3}{7}\sqrt{\frac{5}{\pi}}, \qquad (3.17e)$$

$$G_{22}^{2220} = -\frac{3}{7}\sqrt{\frac{5}{\pi}}, \qquad (3.17f)$$

$$G_{22}^{1111} = -\frac{1}{10}\sqrt{\frac{30}{\pi}}. \qquad (3.17g)$$

The expansion coefficients obtained thus far are complex. To address this issue, we introduce the polar coordinate expression of complex numbers and rewrite the coefficients as follows.

$$c_{11} = \rho e^{i\nu}, \qquad (3.18a)$$
$$c_{20} = Z, \qquad (3.18b)$$
$$c_{22} = \mu e^{i\lambda}, \qquad (3.18c)$$

We consider terms up to $l = 2$ which yield non-zero flow fields on the horizontal plane in Eq. (3.14). This corresponds to considering only the direct interactions between the terms that contribute to the two-dimensional motion in the three-dimensional

space. By substituting s_{lm} with $-\gamma c_{lm}$, we obtain the following system of ordinary differential equations.

$$\frac{d\rho}{dt} = -\frac{3}{10R}\sqrt{\frac{5}{\pi}}(C_1 + C_2)\left(-\sqrt{6}\rho\mu\cos(\lambda - 2\nu) + \rho Z\right) - \left(\alpha + \frac{2D}{R^2}\right)\rho + \frac{\alpha\beta}{4}\sqrt{\frac{6}{\pi}},$$

$$(3.19a)$$

$$\frac{d\nu}{dt} = \frac{3}{10R}\sqrt{\frac{30}{\pi}}(C_1 + C_2)\mu\sin(\lambda - 2\nu),$$

$$(3.19b)$$

$$\frac{dZ}{dt} = \frac{1}{35R}\sqrt{\frac{5}{\pi}}(7C_1\rho^2 + 15C_2 Z^2 - 30C_2\mu^2) - \left(\alpha + \frac{6D}{R^2}\right)Z - \frac{\alpha\beta}{4}\sqrt{\frac{5}{\pi}},$$

$$(3.19c)$$

$$\frac{d\mu}{dt} = \frac{1}{40}\sqrt{\frac{30}{\pi}}\left(-\frac{4C_1\rho^2}{R} + 5\alpha\beta\right)\cos(\lambda - 2\nu) - \frac{6}{7R}\sqrt{\frac{5}{\pi}}C_2 Z\mu - \left(\alpha + \frac{6D}{R^2}\right)\mu,$$

$$(3.19d)$$

$$\frac{d\lambda}{dt} = -\frac{1}{40}\sqrt{\frac{30}{\pi}}\left(-\frac{4C_1\rho^2}{R} + 5\alpha\beta\right)\frac{\sin(\lambda - 2\nu)}{\mu},$$

$$(3.19e)$$

where

$$C_1 = \frac{\gamma}{2\eta + 3\hat{\eta}},$$

$$(3.20a)$$

$$C_2 = \frac{\gamma}{5(\eta + \hat{\eta})}.$$

$$(3.20b)$$

Because this system is in a dimensional form, it is difficult to directly compare it with the experimental results. A more useful system is obtained by non-dimensionalization. We normalize as follows to obtain the system in Eqs. (3.1):

$$\bar{t} = \alpha t,$$

$$(3.21a)$$

$$\bar{\rho} = \rho/\beta,$$

$$(3.21b)$$

$$\bar{Z} = Z/\beta,$$

$$(3.21c)$$

$$\bar{\mu} = \mu/\beta,$$

$$(3.21d)$$

$$\bar{R} = R/l_a.$$

$$(3.21e)$$

After the non-dimensionalization, we obtain a system of ordinary differential equations with three parameters $\bar{R}$, L and $\chi = C_2/C_1 = (2\eta + 3\hat{\eta})/(5\eta + 5\hat{\eta})$. The parameter $L = l_d/l_a$ is determined using constants $l_d = \sqrt{D/\alpha}$ and $l_a = \gamma\beta/\alpha(2\eta + 3\hat{\eta})$, corresponding to the characteristic lengths of diffusion and advection, respectively. When it is possible to estimate the values, the original parameters and variables with dimensions are also used for comparison with the experimental values. Note that the delta function of the supply term in Eq. (3.2) is smoothed out in this approximation.

3.2.4   Approximation to the first degree

If we consider the first-degree approximation within the spherical harmonics expansion, we obtain the following model of the droplet motion:

$$\frac{d\bar{\rho}}{dt} = -\left(\alpha + \frac{2D}{R^2}\right)\left(\bar{\rho} - \frac{1}{4}\sqrt{\frac{6}{\pi}}\frac{\alpha}{\alpha + \frac{2D}{R^2}}\right), \qquad (3.22a)$$

$$\frac{d\nu}{dt} = 0. \qquad (3.22b)$$

While it only shows stable straight motion, all of its parameters can be estimated from the experiments.

Because $s_1^1 = -\gamma\beta\bar{\rho}e^{i\nu}$ and $s_1^{-1} = \gamma\beta\bar{\rho}e^{-i\nu}$, the velocity of the droplet is given in terms of the variables $\bar{\rho}$ and ν as

$$\mathbf{v}^D = -\sqrt{\frac{1}{6\pi}}\frac{2\gamma\beta\bar{\rho}}{2\eta + 3\hat{\eta}}\begin{pmatrix} \cos\nu \\ -\sin\nu \\ 0 \end{pmatrix}, \qquad (3.23)$$

using Eq. (3.4). Therefore, the equilibrium solutions of Eqs. (3.22) can be used to obtain a formula connecting the radius and the speed of the droplet, which can be further used to estimate the parameter l_d from the experimental results:

$$v(R) = \frac{v_\infty}{1 + \frac{2l_d^2}{R^2}}, \qquad (3.24)$$

where $v_\infty = \gamma\beta/2\pi(2\eta + 3\hat{\eta})$ is the speed of the droplet when R is infinite.

3.3   Numerical simulation

In this section, we introduce random perturbations to the model derived in the previous section and study the effect on motion.

From the analytical study, it has been suggested that the angular response to perturbations in the direction of motion changes according to the droplet size under a certain range of model parameters [19]. The rate of increase of the deviation from the stable equilibrium solution with the straight motion is defined by $\Delta\nu_\infty = M\Delta\nu_0$ in terms of an initial perturbation $\Delta\nu_0$ and the following response $\Delta\nu_\infty$. The coefficient M is analytically calculated as $M = A_2/(A_2 - 2A_1)$, where $d\nu/d\bar{t} = A_1\sin(\lambda - 2\nu)$ and $d\lambda/d\bar{t} = A_2\sin(\lambda - 2\nu)$ are from Eq. (3.1b) and (3.1e). It has been suggested that the effect of perturbation is suppressed ($M < 1$) when $R \leq 34\ \mu$m and amplified ($M > 1$) when $R \geq 34\ \mu$m under the choice of parameters that are estimated from experimental results (Fig. 3.1). This is mainly caused by the change in droplet size, switching the swimming mode of the stable equilibrium solution from puller to pusher with straight motion. However, the discussion here concerns only single noise events, and it is not obvious whether the overall motion of droplets may be affected in a similar manner.
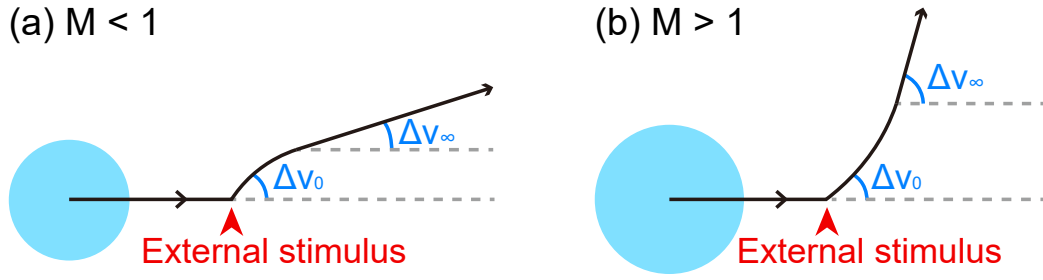
Figure 3.1: Schematic illustrations of motions of droplets under external stimuli with $M < 1$ (a) and $M > 1$ (b).

In this study, we verify whether the angular response to perturbations also affects the global behavior of droplets by performing numerical simulations using the established model with the addition of perturbations. As it is unclear what kind of perturbation is applied to the droplet in the experiments, we will add random perturbations of different natures, and observe how the motion is affected.

Here, we assume that the effect of perturbation is rapidly reflected in the motion of the droplet, and consequently, the overall distribution of the concentration of surfactant on the surface remains unchanged. Accordingly, the perturbation is introduced only to the direction of motion, which corresponds to adding a noise term to the time evolution of ν.

In the experimental settings, two possible origins of perturbations to the motion of droplets have been suggested in literature. One is the thermal noise of the concentration field [23, 22] and the other is the chemical trails [21, 24]. To simulate their characteristics, we consider two scenarios for random perturbations. The thermal noise is modeled by the white noise of the form $A_w \xi$, where A_w represents the strength of noise and ξ is the Gaussian white noise. We introduce a kind of sporadic noise to mimic the perturbation that is caused by the chemical trails. More specifically, we use the perturbation term of the following form:

$$\sum_{k=1}^{N} a_k \exp\left(-(t - t_k)^2 / w^2\right), \tag{3.25}$$

where a_k is uniformly distributed on $-A_s \leq a_k \leq A_s$, t_k is uniformly distributed across the considered time interval $0 \leq t \leq T$, and w is the occurring time of a single perturbation event. In this case, the time average of the noise is expected to be 0 and its variance is approximately $\sqrt{\frac{\pi}{2}} \frac{A_s^2 N}{3T}$. For the analysis below, we use the frequency of noise events $f = N/T$ instead of N.

The numerical simulations were performed under choice of parameters $\chi = 0.41$ and $L = 0.0082$, which are the same values used in the previous study of a water-in-oil droplet system [19]. The parameter $\chi = (2\eta + 3\hat{\eta})/(5\eta + 5\hat{\eta})$ is calculated as 0.41 using the values of the viscosity of squalane 28.33×10^{-3} kg/(m·s) [57] and water 0.89×10^{-3} kg/(m·s) (0.1 MPa, 25 °C). The parameter $L = D/2\pi L v_\infty l_d$ is calculated

as 0.0082 by fitting the speed of droplets with Eq. (3.24) using experimental results. The initial values are chosen to be those of the stable equilibrium solutions for straight motion at each radius. For the model with white noise perturbations, the numerical simulation was conducted using the Euler–Maruyama scheme with a time step $\Delta t = 0.001$. The model with sporadic noise was integrated numerically using the Runge–Kutta method with a time step $\Delta t = 0.001$. The choice of timestep does not affect the results substantially as qualitatively similar results are obtained when we halved the timestep.

In summary, the model with random perturbation has the following form:

$$\frac{d\bar{\rho}}{d\bar{t}} = -\frac{3}{10\bar{R}}\sqrt{\frac{5}{\pi}}(1+\chi)\left(-\sqrt{6}\bar{\rho}\bar{\mu}\cos(\lambda-2\nu)+\bar{\rho}\bar{Z}\right) - \left(1+\frac{2L^2}{\bar{R}^2}\right)\bar{\rho} + \frac{1}{4}\sqrt{\frac{6}{\pi}}$$
(3.26a)

$$\frac{d\nu}{d\bar{t}} = \frac{3}{10\bar{R}}\sqrt{\frac{30}{\pi}}(1+\chi)\bar{\mu}\sin(\lambda-2\nu) + \text{Noise}$$
(3.26b)

$$\frac{d\bar{Z}}{d\bar{t}} = \frac{1}{35\bar{R}}\sqrt{\frac{5}{\pi}}(7\bar{\rho}^2+15\chi\bar{Z}^2-30\chi\bar{\mu}^2) - \left(1+\frac{6L^2}{\bar{R}^2}\right)\bar{Z} - \frac{1}{4}\sqrt{\frac{5}{\pi}}$$
(3.26c)

$$\frac{d\bar{\mu}}{d\bar{t}} = \frac{1}{40}\sqrt{\frac{30}{\pi}}\left(-\frac{4\bar{\rho}^2}{\bar{R}}+5\right)\cos(\lambda-2\nu) - \frac{6}{7\bar{R}}\sqrt{\frac{5}{\pi}}\chi\bar{Z}\bar{\mu} - \left(1+\frac{6L^2}{\bar{R}^2}\right)\bar{\mu}$$
(3.26d)

$$\frac{d\lambda}{d\bar{t}} = -\frac{1}{40}\sqrt{\frac{30}{\pi}}\left(-\frac{4\bar{\rho}^2}{\bar{R}}+5\right)\frac{\sin(\lambda-2\nu)}{\bar{\mu}} :$$
(3.26e)

where the noise term was either white noise or a term of the form of Eq. (3.25). For comparison, we also consider simulations without the deterministic model terms. In this case, we numerically analyzed the following equations, which can be considered as that of an active Brownian swimmer with only rotational diffusion when the noise term is a white noise [63].

$$\frac{d\bar{\rho}}{d\bar{t}} = \frac{d\bar{Z}}{d\bar{t}} = \frac{d\bar{\mu}}{d\bar{t}} = \frac{d\lambda}{d\bar{t}} = 0,$$
(3.27a)

$$\frac{d\nu}{d\bar{t}} = \text{Noise}.$$
(3.27b)

3.3.1   Response to random perturbations

First, the white noise of the form $A_w\xi$ was introduced as a perturbation, and numerical simulations were performed with $A_w = 1$. The results are shown in Fig. 3.2. The trajectories of the centroids demonstrate that, when the model is included, the trajectory tends to bend less when $M < 1$ ($R = 18$ μm), whereas it tends to bend more when $M > 1$ ($R = 50$ μm) (Fig. 3.2 (a-1)(b-1)). This effect is also confirmed through angular autocorrelation. We calculated the angular autocorrelation function of the direction of motion of the droplets with velocity $\mathbf{v^D}(t)$, which is given as a function of lag time τ: $\langle C(t,\tau)\rangle_t = \left\langle \frac{\mathbf{v^D}(t+\tau)\cdot\mathbf{v^D}(t)}{|\mathbf{v^D}(t+\tau)||\mathbf{v^D}(t)|} \right\rangle_t$, where $\langle\rangle_t$ represents the time

average, and a three-point moving average is applied to the velocity. The results show that for $M < 1$ ($R = 18$ μm), the decrease of angular autocorrelation in the case with the model is more suppressed whereas for $M > 1$ ($R = 50$ μm), it is more amplified compared to the model-less case (Fig. 3.2 (a-2)(b-2)).

Next, the sporadic noise was introduced as a perturbation, and numerical simulations were performed using $f = 0.05, w = 5$, and $A_s = 5$. The results are shown in Fig. 3.3 and were similar to those obtained using white noise; however, the detailed characteristics of the trajectories were different. In the case of white noise, the accumulation of small perturbations results in a winding motion, whereas in the case of sporadic noise, the direction of motion changed smoothly. It can be seen that the characteristics of the noise are properly reflected in the motion.

3.3.2 Effect of changes in frequency of noise events on the droplet motion

In experiments, it has been observed that a straight-to-curvilinear motion transition occurs as the droplet radius increases [19]. A larger droplet radius is expected to increase the frequency of encounters with noise sources or events, because it also increases the speed and the surface area of the droplet. Therefore, we conducted numerical simulations with varying values of f, which controls the frequency of noise events. The results with $R = 100$ μm, $A_s = 5$, $w = 5$, and $f = 0.05$ or 0.5 are shown in Fig. 3.4. For the trajectories of the centroid, the increased frequency results in more curly trajectories (Fig. 3.4 (a)(b)). Fig. 3.4 (c) also shows the increased decay in angular autocorrelation as f increases. Notably, each plot shows oscillatory behavior when $f = 0.5$ although this effect is smoothed out and only a monotonous decay is observable in the plot of the ensemble average. The oscillatory behavior is also present in the experiments in the previous study when the droplet size is large [19].

3.4 Conclusion

We analyzed various types and properties of noise that are directly applied on the motion direction of the droplet. Numerical simulations with the addition of perturbation confirmed the suppression and amplification of angular response suggested by the analysis [19].

The numerical simulations of droplet motion with different types of noise, assuming thermal noise (white noise) and noise due to intermittent stimuli such as chemical trails (sporadic noise), demonstrated that the detailed characteristics of the trajectories were different, although overall, they are similar. This indicates that the model widely contributes to the average properties of the motion, e.g. persistency of the straight motion [20, 46, 19, 21].

The results of the numerical simulation when varying the frequency of sporadic noise events f were consistent with the experimental results of the larger-sized droplet, in that more curly trajectories and more oscillatory angular autocorrelation
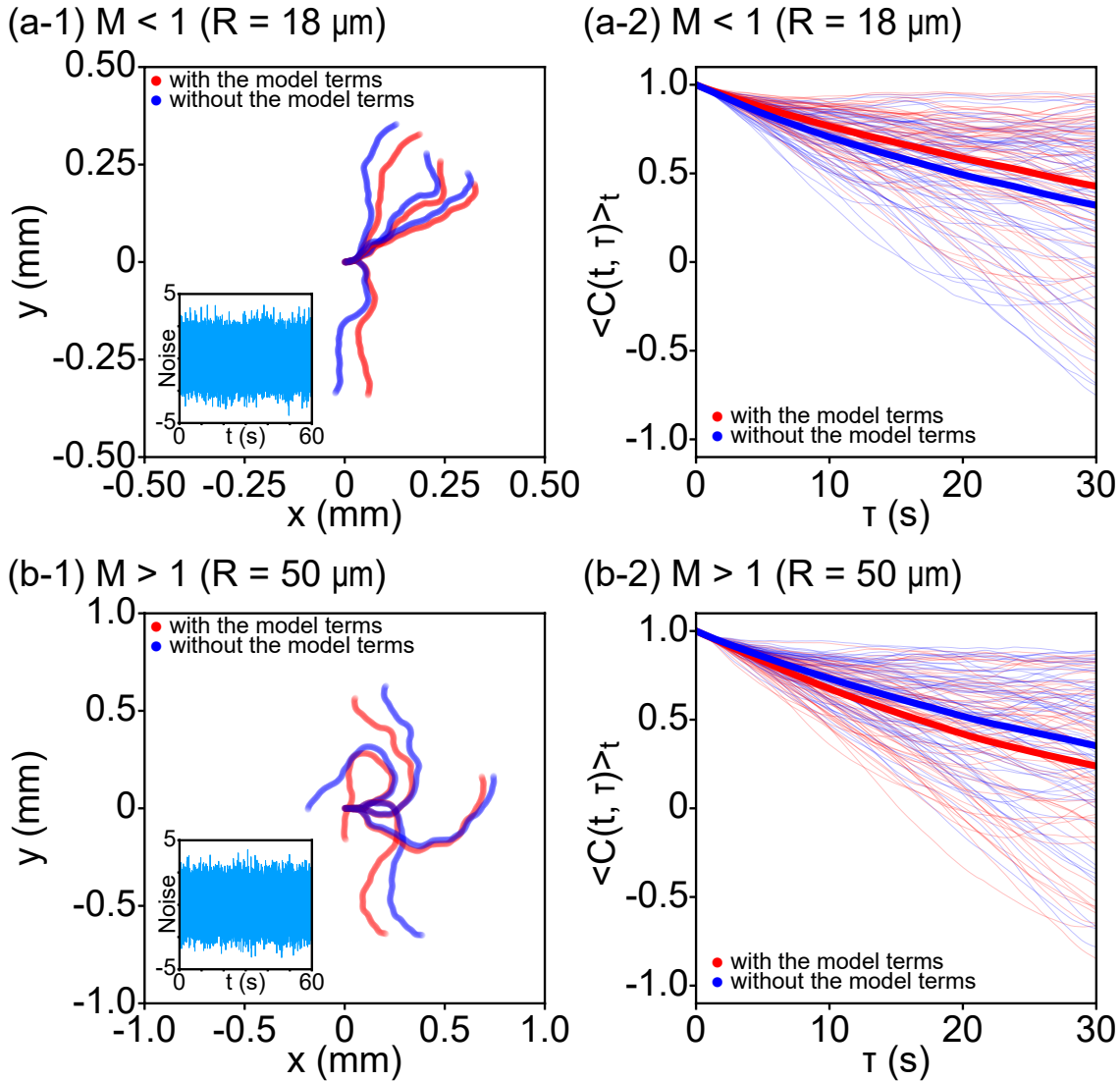
(a-1) M < 1 (R = 18 μm)

(a-2) M < 1 (R = 18 μm)

(b-1) M > 1 (R = 50 μm)

(b-2) M > 1 (R = 50 μm)

Figure 3.2: Results of the numerical simulation with Noise $= A_w \xi$ with or without the present deterministic model terms. Here, the parameter is set to $A_w = 1$. (a) Results of $M < 1$ ($R = 18 \, \mu m$). (b) Results of $M > 1$ ($R = 50 \, \mu m$). (a-1)(b-1) Plots of trajectories of droplet centroids over 60 s for 4 couples of samples. Starting points are set to the origin. Red or blue plots indicate the results with or without the model terms, respectively. Insets: Samples of time series data of the noise added. (a-2)(b-2) Plot of angular autocorrelation function $\langle C(t, \tau) \rangle_t$ of the direction of motion of the droplets for 64 samples. Red or blue plots indicate the results with or without the model terms, respectively. Thin lines correspond to the individual droplets, and the thick lines show the ensemble averages of the droplets.

(a-1) M < 1 (R = 18 μm)

(a-2) M < 1 (R = 18 μm)

(b-1) M > 1 (R = 50 μm)

(b-2) M > 1 (R = 50 μm)

Figure 3.3: Results of numerical simulation with Noise = $\sum_{k=1}^{N} a_k \exp\left(-(t-t_k)^2/w^2\right)$ with or without the present deterministic model terms. Here, parameters are $f = 0.05, A_s = 5$, and $w = 5$. (a) Results of $M < 1$ ($R = 18 \ \mu m$). (b) Results of $M > 1$ ($R = 50 \ \mu m$). (a-1)(b-1) Plots of trajectories of droplet centroids over 60 s for 4 couples of samples. Starting points are set to the origin. Red or blue plots indicate the results with or without the model terms, respectively. Insets: Samples of time series data of the noise added. (a-2)(b-2) Plot of angular autocorrelation function $\langle C(t,\tau)\rangle_t$ of the direction of motion of the droplets for 64 samples. Red or blue plots indicate the results with or without the model terms, respectively. Thin lines correspond to the individual droplets, and the thick lines show the ensemble averages of the droplets.
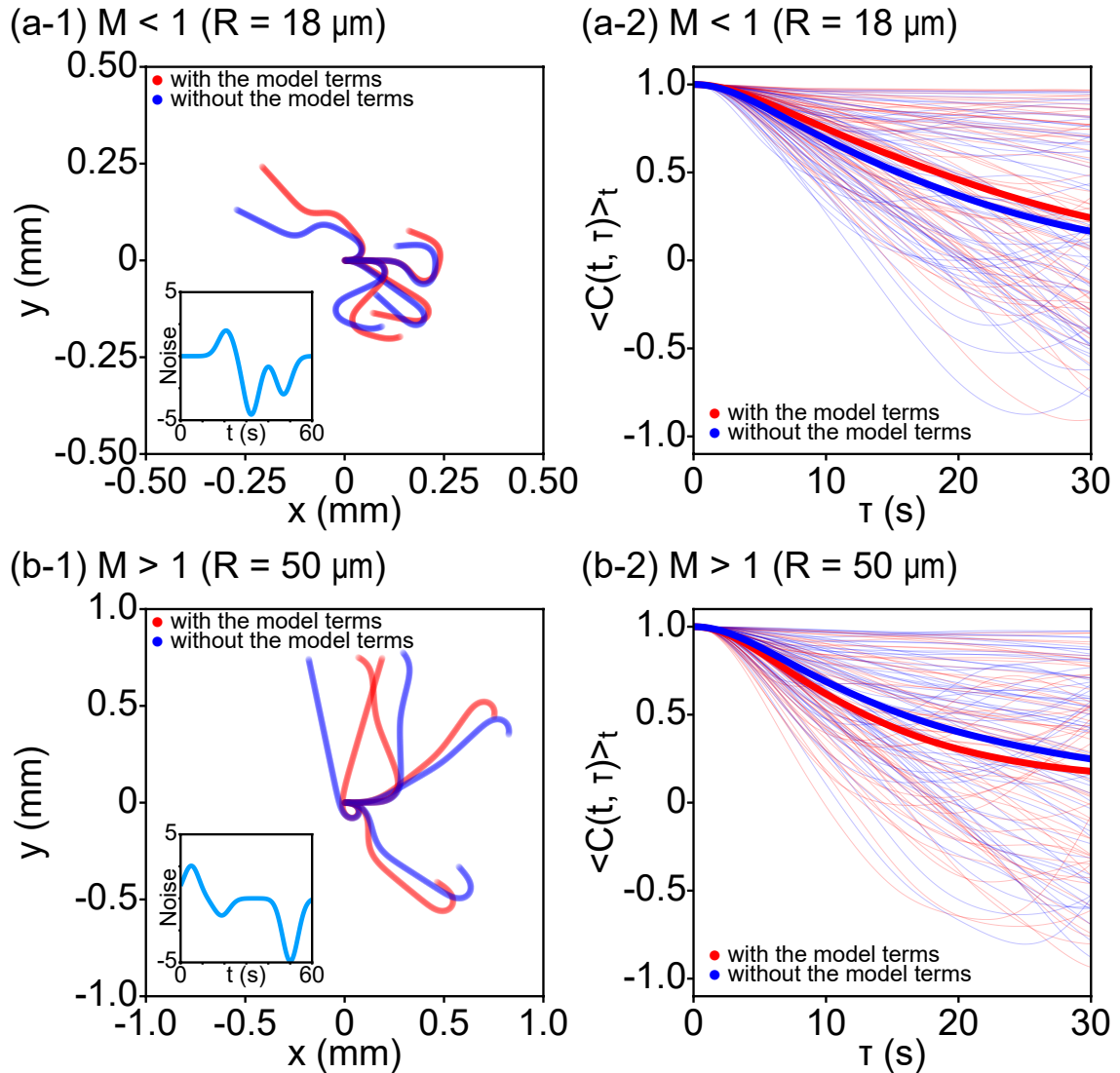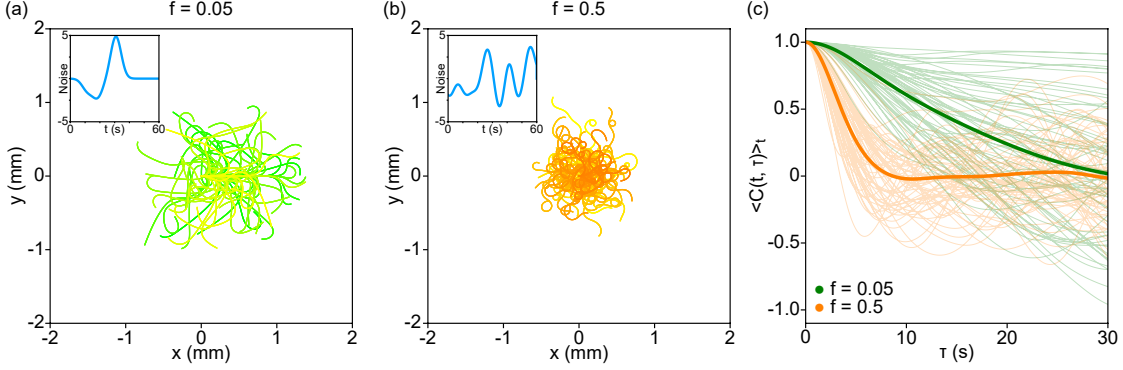
Figure 3.4:   Results   of   numerical   simulation   with   Noise $=$
$\sum_{k=1}^{N} a_k \exp\left(-(t - t_k)^2/w^2\right)$ for varying values of f.   Other parameters are
set to $R = 100 \ \mu m$, $A_s = 5$ and $w = 5$. (a)(b) Plots of trajectories of the droplet
centroids over 60 s for 64 samples.   The starting points are set to the origin.
Color variation depicts different droplets. (a) Results of $f = 0.05$. (b) Results of
$f = 0.5$. Insets: Samples of time series data of the noise added. (c) Plot of angular
autocorrelation function $\langle C(t, \tau)\rangle_t$ of the direction of motion of the droplets for
64 samples. Green plots show the results of $f = 0.05$ and orange plots show the
results of $f = 0.5$. The thin lines correspond to the individual droplets, and the
thick lines show the ensemble averages of the droplets.

are observed as f increases. Therefore, it is presumable that the noise experienced
by the droplets in the experimental setting shows similar characteristics to sporadic
noise. It can also be inferred that the increased frequency of noise events, such as
that proportional to R^2 or v^D, contributes to the rotational motion transition that
accompanies the increase in droplet size. Additionally, the results indicate that the
characteristics of the droplet motion are largely dependent on the time scale of the
frequency of noises relative to the response of motion.

Overall, the results obtained suggested that the types and properties of external
perturbation have a considerable effect on the droplet motion. It is noted that
we assumed simplifying hypotheses on the supply and removal of the surfactants
when deriving the model and consequently the interaction with microscopic factors
which act as sources of noises is possibly not modelled faithfully. Another possible
source of noise is the coupling of modes with spherical harmonics of degrees higher
than two, which correspond to fine distribution of surfactants. Therefore, it will be
interesting to clarify the kind of noise that is present in the actual droplet based
on further exploration using experimental and theoretical approaches. Elucidating
the effect of perturbations on droplet motion will be important also for controlling
droplets in engineering applications. Finally, while the nonlinear coupling of higher
degree modes contributes to the magnified effect of noises, it is expected that the
active Brownian model is useful if the approximation to the first degree is effective.
Droplets with smaller radius are examples of such situation and it will be interesting
to compare the experimental results with this simpler model.

3.5 Appendix

Mathematical preliminaries

In this article, the polar coordinates are defined as

$$\mathbf{r} = r \begin{pmatrix} \sin\theta\cos\phi \\ \sin\theta\sin\phi \\ \cos\theta \end{pmatrix}. \tag{3.28}$$

The normal tangent vectors of the unit sphere are given by

$$\mathbf{e}_\theta = \frac{\mathrm{d}\mathbf{r}}{\mathrm{d}\theta}\Big|_{r=1}, \tag{3.29a}$$

$$\mathbf{e}_\phi = \frac{\mathrm{d}\mathbf{r}}{\mathrm{d}\phi}\Big|_{r=1}. \tag{3.29b}$$

Therefore each tangent vector field on the unit sphere has the form

$$\mathbf{u} = u_\theta \mathbf{e}_\theta + u_\phi \mathbf{e}_\phi. \tag{3.30}$$

The Laplacian operator on the sphere is given by

$$\Delta_{\mathrm{sphere}} = \frac{1}{\sin\theta}\frac{\partial}{\partial\theta}\left(\sin\theta\frac{\partial}{\partial\theta}\right) + \frac{1}{\sin^2\theta}\frac{\partial^2}{\partial\phi^2}. \tag{3.31}$$

The spherical harmonic functions are defined by

$$Y_l^m(\theta,\varphi) = \sqrt{\frac{2l+1}{4\pi}\frac{(l-m)!}{(l+m)!}}P_l^m(\cos\theta)e^{im\varphi}, \tag{3.32}$$

where $|m| \leq l$. These are the eigenfunctions of the Laplacian operator and satisfy

$$\Delta_{\mathrm{sphere}}Y_l^m = -l(l+1)Y_l^m. \tag{3.33}$$

Sufficiently well-behaved functions on the sphere can be expanded in terms of the spherical harmonic functions. Namely, a function $c : S^2 \to \mathbb{C}$ can be written as

$$c(\phi,\theta) = \sum_{l,m} c_l^m Y_l^m(\phi,\theta), \tag{3.34}$$

where the coefficients c_l^m are calculated by

$$c_l^m = \int_0^\pi \int_0^{2\pi} c(\phi,\theta)(Y_l^m)^* \sin\theta\,\mathrm{d}\theta\,\mathrm{d}\phi. \tag{3.35}$$

For example, the delta function δ can be expanded as follows:

$$\delta(\theta-\theta_0,\phi-\phi_0) = \sum_{l=0}^\infty \sum_{m=-l}^l \sqrt{\frac{2l+1}{4\pi}\frac{(l-m)!}{(l+m)!}}P_l^m(\cos(\theta_0))e^{-im\phi_0}Y_l^m. \tag{3.36}$$

Chapter 4

General conclusion

4.1 Conclusion

The purpose of this thesis is to contribute to clarifying the mechanism of the motion transition of swimming droplets. First, experiments were conducted in a system of water-in-oil droplets, which is a typical system of swimming droplets. As a result, the emergence of the straight-to-curvilinear motion transition with droplet size, which has not been observed before, was revealed. To clarify the relationship between curvilinear motion and higher hydrodynamic modes, we developed a three-dimensional axis-asymmetric model consisting of the Stokes equation and an advection-diffusion equation with surfactant inflow and outflow terms. This model can be compared with the experimental results by introducing the characteristic quantities of the experimental system as parameters, thus contributing to elucidating the mechanism of the experimentally observed phenomena. Next, applying the parameters of the actual experimental system, analysis and numerical simulations of the model revealed that the angular response to external perturbations varies with droplet size, which in turn affects the global behavior. This is due to the contribution of the higher hydrodynamics modes, which are responsible for the asymmetry with respect to the axis of direction of a droplet. It was suggested that this effect contributes to the straight-to-curvilinear motion transition observed in the experiment. To further discuss how external perturbations contribute to the complex motion of droplets, two different types of noise, the thermal noise modeled by the white noise and a kind of sporadic noise to mimic the perturbation caused by the chemical trails, were added to the model and numerical simulations were performed. The results suggested that the types and characteristics of the noise affect the droplet motion. Numerical simulations were also performed with varying the frequency of each noise event of sporadic noise. The results indicated that the increase in the frequency of noise events is likely to contribute to the curvilinear motion. In particular, it is reasonable to assume such an effect when the droplet size increases. In general, it was indicated that the transition of the swimming droplet motion is due to the contribution of higher hydrodynamic modes and the noise affecting the droplet.

4.2   Future problems

Although third or higher-degree hydrodynamic modes were not considered in this model, the fitting results of the experimentally observed internal convection suggested that higher terms may also exist. We would like to clarify the relationship between the higher-degree terms and the motion.

Another interesting problem is to elucidate the practical effect of noise on the complex motion of the droplet by investigating the actual noise on the droplets. Concerning chemical traces, it has already been shown that chaotic behavior can emerge due to interactions with the traces [21]. As a first step, we would like to investigate more precisely the influence of chemical traces on droplets, which are easier to observe, to approach the detailed mechanism of motion transition of a swimming droplet.

For engineering applications of swimming droplets, it is necessary to investigate the influence of geometric conditions around the droplet on its motion. In a previous study, it has been shown experimentally that the motion changes depending on whether the space is three-dimensional or quasi-two-dimensional [20]. Moreover, the effect of walls on the flow field around a swimming droplet has been studied experimentally and theoretically [64]. Furthermore, the behavior of swimming droplets confined in capillaries with square and circular cross-sections has also been studied [18]. We would like to contribute to engineering applications by furthering the construction and analysis of models that take into account these geometrical conditions.

References

[1] E. Lauga and T. R. Powers. The hydrodynamics of swimming microorganisms. *Reports on Progress in Physics*, 72(9):096601, 2009.

[2] T. Vicsek and A. Zafeiris. Collective motion. *Phys. Rep.*, 517(3):71–140, 2012.

[3] M. C. Marchetti, J. F. Joanny, S. Ramaswamy, T. B. Liverpool, J. Prost, M. Rao, and R. Aditi Simha. Hydrodynamics of soft active matter. *Rev. Mod. Phys.*, 85(3):1143–1189, 2013.

[4] J. Elgeti, R. G. Winkler, and G. Gompper. Physics of microswimmers—single particle motion and collective behavior: a review. *Reports on Progress in Physics*, 78(5):056601, 2015.

[5] I. S. Aranson. Bacterial active matter. *Reports on Progress in Physics*, 85(7):076601, 2022.

[6] H. Ceylan, J. Giltinan, K. Kozielski, and M. Sitti. Mobile microrobots for bioengineering applications. *Lab Chip*, 17:1705–1724, 2017.

[7] B. Jurado-Sánchez and J. Wang. Micromotors for environmental applications: a review. *Environ. Sci.: Nano*, 5:1530–1544, 2018.

[8] E. M. Purcell. Life at low Reynolds number. *American Journal of Physics*, 45(1):3–11, 1977.

[9] C. C. Maass, C. Krüger, S. Herminghaus, and C. Bahr. Swimming droplets. *Annu. Rev. Condens. Matter Phys.*, 7(1):171–193, 2016.

[10] S. Michelin. Self-propulsion of chemically-active droplets, 2022. arXiv: 2204.08953 [physics.flu-dyn].

[11] Z. Izri, M. N. van der Linden, S. Michelin, and O. Dauchot. Self-propulsion of pure water droplets by spontaneous Marangoni-stress-driven motion. *Phys. Rev. Lett.*, 113:248302, 2014.

[12] D. Kagan, R. Laocharoensuk, M. Zimmerman, C. Clawson, S. Balasubramanian, D. Kang, D. Bishop, S. Sattayasamitsathit, L. Zhang, and J. Wang. Rapid delivery of drug carriers propelled and navigated by catalytic nanoshuttles. *Small*, 6(23):2741–2747, 2010.

[13] T. Ban, K. Tani, H. Nakata, and Y. Okano. Self-propelled droplets for extracting rare-earth metal ions. *Soft Matter*, 10:6316–6320, 2014.

[14] T. Ban, M. Sugiyama, Y. Nagatsu, and H. Tokuyama. Motion-based detection of lanthanides (III) using self-propelled droplets. *The Journal of Physical Chemistry B*, 122(46):10647–10651, 2018.

[15] Y. Tu, F. Peng, A. A. M. André, Y. Men, M. Srinivas, and D. A. Wilson. Biodegradable hybrid stomatocyte nanomotors for drug delivery. *ACS Nano*, 11(2):1957–1963, 2017.

[16] C. Jin, C. Krüger, and C. C. Maass. Chemotaxis and autochemotaxis of self-propelling droplet swimmers. *Proceedings of the National Academy of Sciences*, 114(20):5089–5094, 2017.

[17] F. Geyer, M. D'Acunzi, A. Sharifi-Aghili, A. Saal, N. Gao, A. Kaltbeitzel, T-F. Sloot, R. Berger, H-J. Butt, and D. Vollmer. When and how self-cleaning of superhydrophobic surfaces works. *Science Advances*, 6(3):eaaw9727, 2020.

[18] C. de Blois, V. Bertin, S. Suda, M. Ichikawa, M. Reyssat, and O. Dauchot. Swimming droplets in 1D geometries: an active bretherton problem. *Soft Matter*, 17:6646–6660, 2021.

[19] S. Suda, T. Suda, T. Ohmura, and M. Ichikawa. Straight-to-curvilinear motion transition of a swimming droplet caused by the susceptibility to fluctuations. *Phys. Rev. Lett.*, 127:088005, 2021.

[20] M. Suga, S. Suda, M. Ichikawa, and Y. Kimura. Self-propelled motion switching in nematic liquid crystal droplets in aqueous surfactant solutions. *Phys. Rev. E*, 97:062703, 2018.

[21] B. V. Hokmabad, R. Dey, M. Jalaal, D. Mohanty, M. Almukambetova, K. A. Baldwin, D. Lohse, and C. C. Maass. Emergence of bimodal motility in active droplets. *Phys. Rev. X*, 11:011043, 2021.

[22] G. Li. Swimming dynamics of a self-propelled droplet. *Journal of Fluid Mechanics*, 934:A20, 2022.

[23] R. Golestanian, T. B. Liverpool, and A. Ajdari. Propulsion of a molecular machine by asymmetric distribution of reaction products. *Phys. Rev. Lett.*, 94:220801, 2005.

[24] B. V. Hokmabad, J. Agudo-Canalejo, S. Saha, R. Golestanian, and C. C. Maass. Chemotactic self-caging in active emulsions. *Proceedings of the National Academy of Sciences*, 119(24):e2122269119, 2022.

[25] S. Herminghaus, C. C. Maass, C. Krüger, S. Thutupalli, L. Goehring, and C. Bahr. Interfacial mechanisms in active emulsions. *Soft Matter*, 10:7008–7022, 2014.

[26] K. Peddireddy, P. Kumar, S. Thutupalli, S. Herminghaus, and C. Bahr. Solubilization of thermotropic liquid crystal compounds in aqueous surfactant solutions. *Langmuir*, 28(34):12426–12431, 2012.

[27] R. Seemann, J-B. Fleury, and C. C. Maass. Self-propelled droplets. *The European Physical Journal Special Topics*, 225(11):2227–2240, 2016.

[28] M. Schmitt and H. Stark. Marangoni flow at droplet interfaces: Three-dimensional solution and applications. *Phys. Fluids*, 28(1):012106, 2016.

[29] N. Yoshinaga. Simple models of self-propelled colloids and liquid drops: From individual motion to collective behaviors. *Journal of the Physical Society of Japan*, 86(10):101009, 2017.

[30] G. Quincke. Ueber periodische Ausbreitung an Flüssigkeitsoberflächen und dadurch hervorgerufene Bewegungserscheinungen. *Annalen der Physik*, 271(12):580–642, 1888.

[31] B. Otto. *Untersuchungen über mikroskopische Schäume und das Protoplasma; Versuche und Beobachtungen zur Lösung der Frage nach den physikalischen Bedingungen der Lebenserscheinungen.* Leipzig, W. Engelmann, 1892.

[32] Y. Nishigami, M. Ichikawa, T. Kazama, R. Kobayashi, T. Shimmen, K. Yoshikawa, and S. Sonobe. Reconstruction of active regular motion in amoeba extract: Dynamic cooperation between sol and gel states. *PLOS ONE*, 8(8):e70317, 2013.

[33] M. J. Lighthill. On the squirming motion of nearly spherical deformable bodies through liquids at very small Reynolds numbers. *Commun. Pure. Appl. Math.*, 5(2):109–118, 1952.

[34] J. R. Blake. A spherical envelope approach to ciliary propulsion. *J. Fluid Mech.*, 46(1):199–208, 1971.

[35] T. Ohmura, Y. Nishigami, A. Taniguchi, S. Nonaka, J. Manabe, T. Ishikawa, and M. Ichikawa. Simple mechanosense and response of cilia motion reveal the intrinsic habits of ciliates. *Proc. Natl. Acad. Sci. U.S.A.*, 115(13):3231–3236, 2018.

[36] Y. Nishigami, T. Ohmura, A. Taniguchi, S. Nonaka, J. Manabe, T. Ishikawa, and M. Ichikawa. Influence of cellular shape on sliding behavior of ciliates. *Commun. Integr. Biol.*, 11(4):e1506666, 2018.

[37] P-G. de Gennes, F. Brochard-Wyart, and D. Quéré. *Capillarity and Wetting Phenomena.* 2004.

[38] S. Ramaswamy. The mechanics and statistics of active matter. *Annu. Rev. Condens. Matter Phys.*, 1(1):323–345, 2010.

[39] Y. Sumino, N. Magome, T. Hamada, and K. Yoshikawa. Self-running droplet: Emergence of regular motion from nonequilibrium noise. *Phys. Rev. Lett.*, 94(6):068301, 2005.

[40] R. Shimizu and H. Tanaka. A novel coarsening mechanism of droplets in immiscible fluid mixtures. *Nat. Commun.*, 6(7407):7407, 2015.

[41] S. Katsura, A. Yamaguchi, N. Harada, K. Hirano, and A. Mizuno. Microreactors based on water-in-oil emulsion. In *Conference Record of the 1999 IEEE Industry Applications Conference. Thirty-Forth IAS Annual Meeting (Cat. No.99CH36370)*, volume 2, pages 1124–1129, 1999.

[42] E. Verneuil, M. L. Cordero, F. Gallaire, and C. N. Baroud. Laser-induced force on a microfluidic drop: Origin and magnitude. *Langmuir*, 25(9):5127–5134, 2009.

[43] M. Ichikawa, F. Takabatake, K. Miura, T. Iwaki, N. Magome, and K. Yoshikawa. Controlling negative and positive photothermal migration of centimeter-sized droplets. *Phys. Rev. E*, 88:012403, 2013.

[44] J. Čejková, M. Novák, F. Štěpánek, and M. M. Hanczyc. Dynamics of chemotactic droplets in salt concentration gradients. *Langmuir*, 30(40):11937–11944, 2014.

[45] S. Thutupalli, R. Seemann, and S. Herminghaus. Swarming behavior of simple model squirmers. *New J. Phys.*, 13(7):073021, 2011.

[46] A. Izzet, P. G. Moerman, P. Gross, J. Groenewold, A. D. Hollingsworth, J. Bibette, and J. Brujic. Tunable persistent random walk in swimming droplets. *Phys. Rev. X*, 10:021035, 2020.

[47] C. Krüger, G. Klös, C. Bahr, and C. C. Maass. Curling liquid crystal microswimmers: A cascade of spontaneous symmetry breaking. *Phys. Rev. Lett.*, 117:048003, 2016.

[48] T. Yamamoto and M. Sano. Chirality-induced helical self-propulsion of cholesteric liquid crystal droplets. *Soft Matter*, 13(18):3328–3333, 2017.

[49] M. Morozov and S. Michelin. Orientational instability and spontaneous rotation of active nematic droplets. *Soft Matter*, 15:7814–7822, 2019.

[50] F. Takabatake, N. Magome, M. Ichikawa, and K. Yoshikawa. Spontaneous mode-selection in the self-propelled motion of a solid/liquid composite driven by interfacial instability. *J. Chem. Phys.*, 134(11):114704, 2011.

[51] F. Takabatake, K. Yoshikawa, and M. Ichikawa. Communication: Mode bifurcation of droplet motion under stationary laser irradiation. *J. Chem. Phys.*, 141(5):051103, 2014.

[52] K. H. Nagai, F. Takabatake, Y. Sumino, H. Kitahata, M. Ichikawa, and N. Yoshinaga. Rotational motion of a droplet induced by interfacial tension. *Phys. Rev. E*, 87:013009, 2013.

[53] M. Morozov and S. Michelin. Nonlinear dynamics of a chemically-active drop: From steady to chaotic self-propulsion. *J. Chem. Phys.*, 150(4):044110, 2019.

[54] S. Michelin, E. Lauga, and D. Bartolo. Spontaneous autophoretic motion of isotropic particles. *Phys. Fluids*, 25(6):061701, 2013.

[55] W. Thielicke and E. J. Stamhuis. PIVlab towards user-friendly, affordable and accurate digital particle image velocimetry in matlab. *open research software*, 2(1):e30, 2014.

[56] W. T. Coffey and Y. P. Kalmykov. *The Langevin Equation: With Applications To Stochastic Problems In Physics, Chemistry And Electrical Engineering (Fourth Edition).* World Scientific Series In Contemporary Chemical Physics. World Scientific Publishing Company, 2017.

[57] M. J. P. Comuñas, X. Paredes, F. M. Gaciño, J. Fernández, J. P. Bazile, C. Boned, J. L. Daridon, G. Galliero, J. Pauly, K. R. Harris, M. J. Assael, and S. K. Mylona. Reference correlation of the viscosity of squalane from 273 to 373 K at 0.1 MPa. *J. Phys. Chem. Ref. Data*, 42(3):033101, 2013.

[58] A. Farutin, S. Rafaï, D. K. Dysthe, A. Duperray, P. Peyla, and C. Misbah. Amoeboid swimming: A generic self-propulsion of cells in fluids by means of membrane deformations. *Phys. Rev. Lett.*, 111:228102, 2013.

[59] N. P. Barry and M. S. Bretscher. Dictyostelium amoebae and neutrophils can swim. 107(25):11376–11380, 2010.

[60] E. J. Campbell and P. Bagchi. A computational model of amoeboid cell swimming. *Physics of Fluids*, 29(10):101902, 2017.

[61] H. Bruus. *Theoretical Microfluidics.* Oxford Master Series in Physics. 2008.

[62] J. Zhang, B. A. Grzybowski, and S. Granick. Janus particle synthesis, assembly, and application. *Langmuir*, 33(28):6964–6977, 2017.

[63] G. Volpe and S. Gigan. Simulation of the active Brownian motion of a microswimmer. *American Journal of Physics*, 82(7):659–664, 2014.

[64] C. de Blois, M. Reyssat, S. Michelin, and O. Dauchot. Flow field around a confined active droplet. *Phys. Rev. Fluids*, 4:054001, 2019.

Acknowledgement

I would like to express my appreciation to my supervisor Dr. Masatoshi Ichikawa for his helpful advice and support in my studies and student life. He let me do what I wanted to do and gave me many opportunities for learning, participating in conferences, and collaborating. I also would like to thank Dr. Tomoharu Suda (Keio University) and Dr. Takuya Ohmura (University of Basel). They gave me educational instructions and useful advice.

I studied at ESPCI Paris for several months in my Ph. D. course supported by Prof. Olivier Dauchot and Dr. Charlotte de Blois (present affiliation: École Normale Supérieure de Lyon). I would like to express my gratitude to them.

I am grateful to Prof. Hiroyuki Kitahata (Chiba University), Prof. Yasuhiro Kimura (Kyushu University), Prof. Yutaka Sumino (Tokyo University of Science), Prof. Makito Miyazaki, Dr. Yukinori Nishigami (Hokkaido University), Dr. Hiroaki Ito (Chiba University), Dr. Yuki Koyano (Kobe University), Dr. Ikumi Hayakawa, Mr. Masaki Konosu, Mr. Masahiro Makuta, Mr. Hisanori Fujiwara, Mr. Ryota Takenaka, Mr. Masahiro Masuda, Mr. Jungmin An, Mr. Ryoto Imanishi, and Ms. Mariko Suga for fruitful discussion and great comments. I am thankful to all the people who discussed with me at each conference.

I would like to express my thankfulness to Mitsubishi Research Institute for encouraging me to write this thesis.

Finally, I give a special thanks to my partner for always supporting me.